

Neogene and Quaternary ignimbrites in the area of Arequipa, Southern Peru: Stratigraphical and petrological correlations

Perrine Paquereau Lebti ^{a,*}, Jean-Claude Thouret ^a, Gerhard Wörner ^b, Michel Fornari ^c

^a *Laboratoire Magmas et Volcans, Université Blaise Pascal et CNRS, 63038 Clermont-Ferrand, France*

^b *GZG, Abt. Geochemie, Goldschmidstrasse 1, Universität Göttingen, 37077 Göttingen, Germany*

^c *IRD, UMR Géosciences Azur, Sophia Antipolis, Parc Valrose, 06108 Nice cedex 2, France*

Received 22 September 2005; received in revised form 14 February 2006; accepted 20 February 2006

Available online 5 May 2006

Abstract

This study focuses on the correlation of four newly identified rhyolitic ignimbrites located around Arequipa, which were previously described as a single ignimbrite sheet: (1) The Río Chili Ignimbrite (ca. 13.33 Ma) crops out in the Río Chili canyon and consists of a cooling unit of non-welded to partially welded, massive, crystal-rich lapilli tuff. This ignimbrite represents the base of the Neogene ignimbrite succession in the Arequipa area and may be stratigraphically equivalent to the 14–13 Ma Huaylillas Ignimbrites in southern Peru. (2) The second voluminous (~20 km³) and widespread La Joya Ignimbrite sheet (ca. 4.87 Ma) filled the Arequipa depression. Its probable source is now buried underneath the Chachani volcanic complex. The La Joya Ignimbrite covers both the Arequipa Batholith toward the Río Vitor piedmont and also part of the Altiplano to the East and North of the Chachani complex. (3) The Arequipa Airport Ignimbrite (AAI) sheet (ca. 1.6 Ma, ~18 km³), the third and latest infill of the Arequipa basin, consists of a lower white, columnar jointed, massive lapilli tuff, indurated by vapor-phase recrystallization, and is overlain by an upper, pink, lithic-rich, non-welded, massive lapilli-tuff. The source of this ignimbrite is also buried underneath the Chachani complex, as indicated by anisotropy of magnetic susceptibility measurements and component lithology. (4) The Yura non-welded pumice-flow deposits (ca. 1.02 Ma, 1.5 km³) are restricted to the northern and western flanks of the Chachani complex and may correlate with tuffs of the Capillune Formation on the Altiplano.

All ignimbrites are high-K calc-alkaline to alkaline rhyolites, which contain variable amounts of plagioclase, biotite, quartz, sanidine, and Fe–Ti oxides. The modal composition of mineral phases and chemistry of amphiboles and biotites are useful for distinguishing the ignimbrites. Specific geochemical fingerprints, such as Sr, Y, Rb, Ba, Cs, REE, and Sr isotopes were effective discriminator elements. Magmatic differentiation, crustal residence time and contamination, and source melting processes are discussed in order to explain compositional variations. The older La Joya Ignimbrite and Río Chili Ignimbrite reflect initial wetter crustal melts closer to granite composition, whereas with time the younger Arequipa Airport Ignimbrite and Yura Tuffs initial melts are slightly less evolved and dryer due to more extensive crustal melting. The voluminous (>40 km³) Neogene ignimbrites of the Arequipa area were produced by three major explosive volcanic pulses in the Central Volcanic Zone of southern Peru, whose genetic relation with tectonic uplift and crustal thickening of the Andean Cordillera are still a matter of debate.

© 2006 Elsevier B.V. All rights reserved.

Keywords: ignimbrite; Peru; stratigraphy; ⁴⁰Ar–³⁹Ar ages; petrology; correlation

* Corresponding author. Tel.: +33 4 73 34 67 21; fax: +33 4 73 34 67 44.

E-mail address: P.Paquereau@opgc.univ-bpclermont.fr (P.P. Lebti).

1. Introduction

Voluminous Neogene and Quaternary ignimbrites occur in the Arequipa Province, of the Central Volcanic Zone of the Andes in southern Peru (Fig. 1A). Volcanic activity has played an important role in southern Peru since the Late Cretaceous/early Paleocene and is related to subduction of the Nazca plate below the South America continental plate (Lefèvre, 1979; Sébrier et al., 1988; Mercier et al., 1992). Subduction and upper plate

shortening resulted in crustal thickening and high crustal temperatures. Three main periods of magmatic activity have been identified: Late Cretaceous–Paleocene (Toquepala Group), early to mid-Miocene (Tacaza and Huaylillas Formations) and upper Miocene to Quaternary (Sencca Formation and Barroso Group). Neogene ignimbrite sheets in the Arequipa area are therefore in part stratigraphic equivalents of the Huaylillas and Sencca ignimbrites observed in southern Peru (Lefèvre, 1979; Thouret et al., 2004).

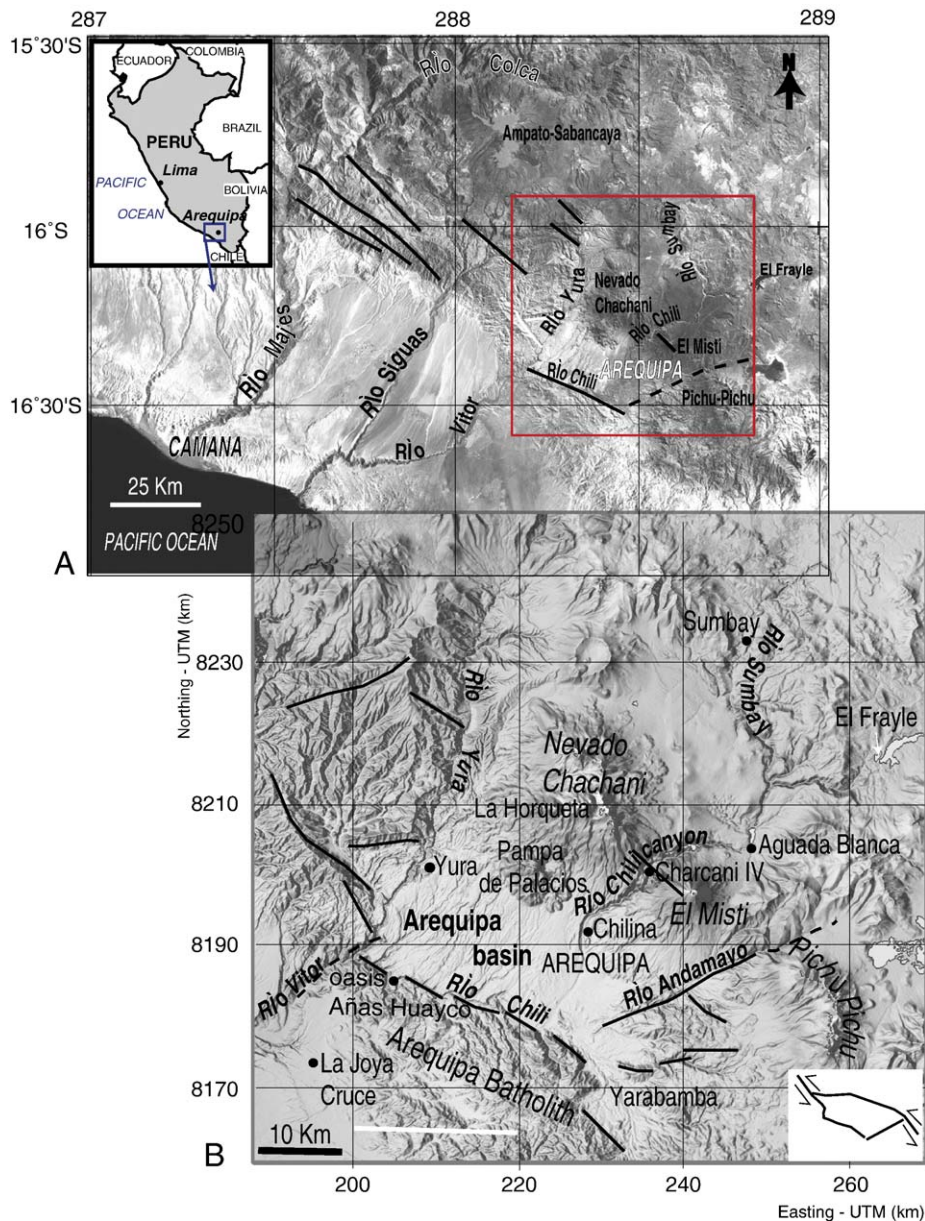


Fig. 1. (A) Landsat image (1996) of south-western Peru and (B) DEM of the Arequipa area (from the USGS web site), showing locations quoted in the text. In (B) straight lines are main faults and dashed lines are inferred faults. Inset: sketch of the tectonic setting of the Arequipa basin.

Locally, the ignimbrites of Arequipa are termed “sillar”. Fenner (1948) first introduced this term in the volcanological literature when describing the well-known whitish ignimbrite used for construction of colonial buildings in Arequipa. Construction blocks are indurated by vapor-phase recrystallization, in contrast to the non-welded ignimbrites elsewhere. Definitions of “sillar” have varied ever since to include either non-welded and non-indurated, or incipiently welded, or partially welded, or indurated by vapor-phase crystallization, as shown in the compilation by Barker (1996). This author concludes that the term sillar is useless for volcanologists because of its too broad meaning and that the term should be abandoned. His suggestion is

justified because the previously described “sillars” in the Arequipa region (Fenner, 1948; Jenks and Goldish, 1956) actually belong to four different individual ignimbrite sheets (Fig. 2), which display significant differences in composition, depositional facies, welding, and age.

In this paper, a “flow unit” is the product of a single pyroclastic flow in one lobe (Fisher and Schmincke, 1984). An ignimbrite sheet or cooling unit, however, comprises an assemblage of associated flow units of the same eruptive sequence. In a simple cooling unit there is evidence, in the form of jointing or welding, that successive flow units were emplaced so quickly that they cooled together with no sharp changes in the

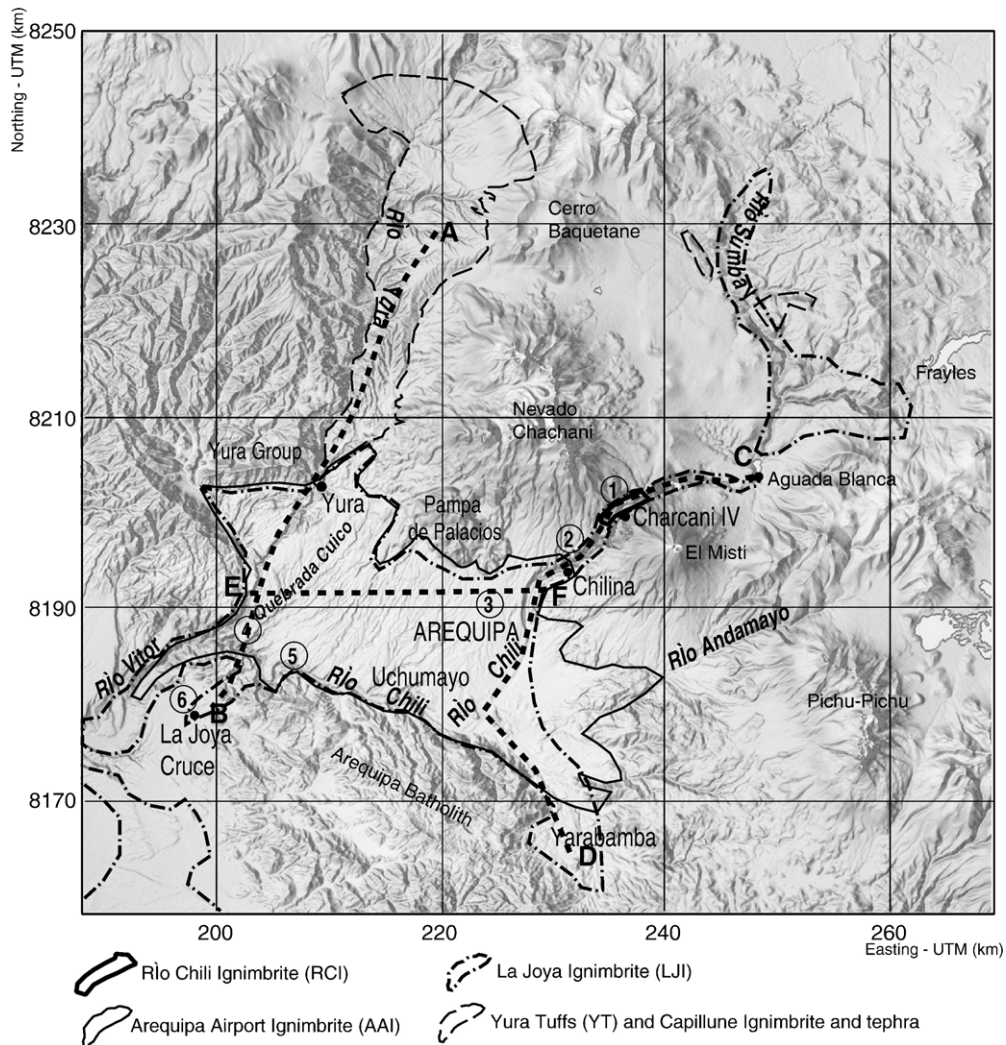


Fig. 2. DEM of the Arequipa area based on digitized maps for the western part and on RADAR interferometry for the eastern part, interpolated with surfer 7 (krigeage gridding method with 30m grid) and draped with the extract of the 1996 Landsat scene. Dashed black and white lines (A–B, C–D and E–F) indicate sections in Fig. 3; circled numbers correspond to the location of stratigraphic sections of Fig. 4. The approximate boundaries of the four ignimbrites are shown.

temperature gradient after their deposition. By contrast, in a compound cooling unit, breaks in temperature disturb the continuous cooling zonation of successive hot flows (Fisher and Schmincke, 1984). In the field, ignimbrites often display various degrees of partial welding, which correspond to the sintering together and flattening of hot clasts to form a denser and more coherent rock (Francis and Oppenheimer, 2004).

Large pyroclastic flow deposits are often difficult to correlate owing to a complex emplacement history, petrologic and chemical heterogeneity, and the Arequipa Ignimbrites are not an exception. Ignimbrites usually display radial and vertical gradation in mean grain size and sorting, zonation in welding and in component proportions, as well as in assemblages and compositions of phenocrysts. In order to fingerprint and correlate as many as four ignimbrite sheets, a combination of criteria (e.g. Hildreth and Mahood, 1985), that includes field observations, stratigraphy, ^{40}Ar – ^{39}Ar chronology, mineralogy, and geochemistry were used. We also tried to locate the sources of the ignimbrites by analyzing the geometry of the deposits and their relations to other geologic structures at a regional scale. We finally discuss how ignimbrite magmatism may be related to uplift and crustal shortening in the Central Andes.

2. Geological setting

The WNW–ESE-trending Arequipa tectonic depression is 30 km long and 15 km wide and is interpreted as a pull-apart basin related to major NW–SE faults (Mering et al., 1996). It is located between the Late Cretaceous (77–59 Ma, Lefèvre, 1979) Arequipa Batholith to the SW (2000 to 2800 masl) and the western Cordillera to the NE (>5000 masl) (Fig. 1B). The strike–slip faults bounding the basin to the south (with a small normal component) cut the Arequipa Batholith (Fig. 1B). The Arequipa basin was formed in Tertiary time. The <1-km-deep canyons of the Río Chili, Río Yura, and Río Andamayo valleys cut the western flank of the western Cordillera and are directed towards the Arequipa depression (Figs. 1B and 2). They merge in the SW into the Río Vitor and Sihuas valleys, which extend to the Pacific Ocean.

The western flank of the Western Cordillera, crowned by three upper Miocene to Quaternary volcanoes (Pichu-Pichu, Nevado Chachani, and El Misti), forms the north-eastern and eastern borders of the Arequipa basin with a height difference to the basin floor of as much as 4 km (Figs. 1B and 2). Between the Río Yura and the Río Chili valleys, the Chachani compound volcanic massif (6057 masl) comprises a

cluster of seven edifices (Forget, 2004). This massif is more eroded than its younger neighbor, El Misti (5822 masl). El Misti is an active volcano, whose summit is 17 km to the NE and 3500 m above the Arequipa City center. El Misti deposits overlie deposits from the Chachani complex to the east of the Río Chili (Figs. 1B and 2). South of Chachani, lava flows of the dome-coulees of Pampa de Palacios (Figs. 1B and 3) overlie the Neogene ignimbrites and early Quaternary tuffs that form the uppermost sequences in the Arequipa depression. The Arequipa basin is limited to the east by the dissected Mio-Pliocene Pichu-Pichu volcanic massif (5510 masl), from which a lava flow has been K–Ar dated at 6.7 Ma (Kaneoka and Guevara, 1984). Pichu-Pichu forms an arcuate ridge open towards the west (Arequipa). The amphitheater is related to a voluminous, 1 Ma debris–avalanche deposit, termed the “Arequipa volcanic landslide” (Legros et al., 2000). This debris–avalanche deposit overlies the ignimbrites in the south-eastern basin. In turn, it is overlain toward the NW by a younger debris–avalanche deposit from El Misti volcano (Thouret et al., 2001). To the west of the Río Yura valley, the Arequipa depression is closed by 800 m high scarps of the Jurassic “Yura Group” sediments (Figs. 1B and 2).

Neogene ignimbrites crop out in the deep Río Yura, Chili, and Vitor valleys as well as in the Arequipa tectonic depression (Figs. 2 and 3). These ignimbrites are not restricted here, but are also found outside the basin in scattered outcrops on top of the Arequipa Batholith and intercalated with the Vitor and Sihuas piedmont deposits to the south and SW of Arequipa (Fig. 2). Ignimbrite sheets also crop out in the upper Río Chili valley as far as 20 km north of Arequipa, in the Río Sumbay valley, which cuts into the Western Cordillera, and also on the western Altiplano further north (Fig. 2).

3. Location and extent of Neogene and Quaternary ignimbrites

We distinguish four ignimbrite sheets in the Arequipa area (Table 1, Figs. 2 and 3), based on new field surveys, interpretation of a digital elevation model (DEM) draped with a Landsat image (Fig. 2), information from three geologic maps (García and Landa, 1968; Guevara, 1969; Vargas, 1970), other previous studies (Jenks and Goldish, 1956; Lefèvre, 1979; Vatin-Pérignon et al., 1996), and six new ^{40}Ar – ^{39}Ar ages. The ignimbrite sheets are: the Miocene Río Chili Ignimbrite, the Pliocene La Joya Ignimbrite, the Plio-Quaternary Arequipa Airport Ignimbrite, and

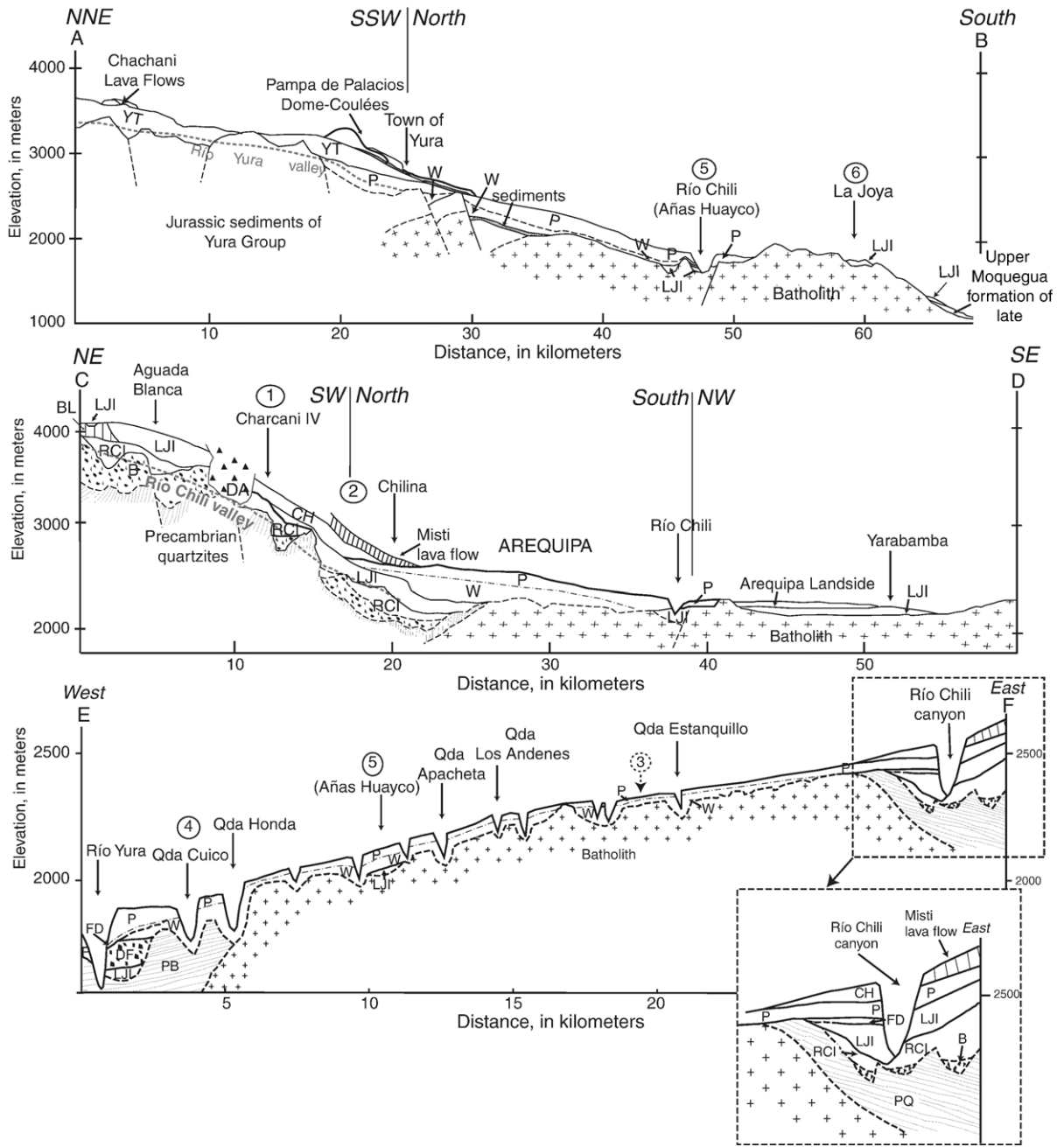


Fig. 3. (A) N–S cross-section of the western part of the Arequipa depression (A–B), (B) N–S cross-section of the eastern part of the depression (C–D), and (C) W–E cross-section of the depression (E–F). Tracks are shown in Fig. 2. PQ: Precambrian quartzite, YGS: Yura Group sediments, B: Breccia, RCI: Río Chili ignimbrite, LJI: La Joya ignimbrite, DF: Debris–flow deposits, BL: Barroso lava flows, W: white unit of the AAI, P: pink unit of the AAI, YT: Yura Tuffs, AL: “Arequipa landslide”, CH: Chachani hydroclastic breccia, DA: debris–avalanche deposits, MLF: El Misti lava flow, FD: tephra–fallout deposit, PB: Pecambrian basement. Circled numbers correspond to location of stratigraphic sections in Fig. 4.

the Quaternary Yura Tuffs and Capillune Formation tuffs (Table 1). The mapped extent of the four ignimbrites is shown in Fig. 2. North–south geologic sections across the Río Yura valley (Fig. 3, A–B) to the west of the Arequipa depression, and across the Río

Chili valley to the east (Fig. 3, C–D), as well as an east–west profile across the depression (Fig. 3, E–F) show the main stratigraphic units.

The inferred areal extent and the estimated thickness of the deposits (ranging from a few meters to 150m),

based on selected stratigraphic sections of the ignimbrite sheets, are used to derive the minimum preserved bulk volume of the four ignimbrite sheets. Results of field work, remote sensing, and geochemical correlations are presented in Table 1 and discussed below.

3.1. The Río Chili Ignimbrite (RCI)

The Miocene Río Chili Ignimbrite (RCI) crops out in the high walls of the upper Río Chili canyon (Charcani IV and Aguada Blanca, Fig. 2), either in unconformable contact with Precambrian quartzites or overlying a previously undescribed diamicton (Fig. 3, Section C–D). The

quartzites and diamicton form a rugged paleotopography which controlled the ignimbrite's emplacement, as shown by an irregular basal part of the deposit. Although the full extent of this ignimbrite is unknown, it was also recognized on the Altiplano north of El Misti volcano where it overlies the Oligocene Tacaza Group. The RCI dips towards the SE beyond the north bank of the Río Chili valley in the area beneath the Quaternary ring plain of El Misti volcano (Figs. 2 and 3). It was not observed in the western part of the Arequipa basin.

Where it can be observed, the RCI averages 70 m in thickness and reaches up to 140 m near the Charcani IV dam (Table 1). In the middle reaches of the Río Chili

Table 1
Characteristics of the Arequipa ignimbrites

Arequipa Ignimbrites	Lithofacies and componentry of vitric tuffs	Preserved extent, average thickness and volume	Welding degree and facies	Mineral assemblage	$^{40}\text{Ar}/^{39}\text{Ar}$ ages in Ma
YT	Stratified ash and pumice flows Pumice and glass shards (pgs) > 80% Free crystals (fc) > 15% Accidental and accessory fragments (aaf) < 5%	Extent ~ 150 km ² Thickness = 10 to 50 m Volume ~ 1.5 km ³ High Aspect Ratio (HAR) ($1.4 \cdot 10^{-3}$)	Non-welded, more or less indurated; no recrystallization	plag. > san. > qz. > biot. > ox.	1.03 ± 0.09 (on biotite)
AAI	Pink unit Lithic-rich massive lapilli-tuff (mLT) pgs > 60% fc > 15% aaf < 25% High content in accidental brownish lava fragments	Extent ~ 600 km ² Thickness = 5 to 100 m Volume = 18 to 20 km ³ HAR ($1.4 \cdot 10^{-3}$)	Non-welded, more or less indurated; no recrystallization	plag. > biot. > ox. > qz. > san. >> amph	1.65 ± 0.04 (on biotite)
	white unit mLT, columnar jointed pgs > 65% fc > 20% aaf < 15%				
LJI	mLT, columnar jointed pgs > 65% fc > 20% aaf < 15%	Extent ~ 800 km ² Thickness = 5 to 80 m Volume ~ 16 to 24 km ³ Middle Aspect Ratio (MAR) ($6.4 \cdot 10^{-4}$)	Non-welded, non-indurated to partially welded, with fiammes and spherulitic features	plag. > san. > qz. > biot. > ox. > amph. devitrification silica phases: cristobalite and tridymite	4.89 ± 0.02 and 4.78 ± 0.21 (on sanidine)
RCI	Crystal-rich mLT pgs < 65% fc > 30% af < 5%	Unknown extent Thickness = 50 to 200 m	Non-welded, indurated to partially welded, with deformed pumices and widespread devitrification	plag. > amph. > biot. > san. > qz. > ox. devitrification silica phases: cristobalite and tridymite	13.19 ± 0.09 (on biotite, average of 3 ages)

YT=Yura Tuffs, AAI=Arequipa Airport Ignimbrite, LJI=La Joya Ignimbrite, RCI=Río Chili Ignimbrite.

(Charcani IV), the ignimbrite's cooling unit comprises at least three flow units. Two samples from two flow units at this locality (Fig. 2) yielded ^{40}Ar – ^{39}Ar ages of 13.39 ± 0.1 and 13.12 ± 0.05 Ma (Table 1). Based on these ages and on its stratigraphic position, the RCI can be correlated with the middle Miocene Huaylillas ignimbrites in southern Peru (Lefèvre, 1979; Wörner et al., 2000; Thouret et al., 2004). The Huaylillas ignimbrites have been dated between 14 and 13.25 Ma west of Arequipa in the Chuquibamba area (Thouret et al., 2004).

3.2. The La Joya Ignimbrite (LJI)

The La Joya Ignimbrite (LJI) crops out in the Arequipa depression, on the Altiplano area as far as 50 km north of Arequipa in the Río Sumbay valley (Fig. 2), and as far as 50 km SW and WSW of Arequipa on the south-western flank of the Arequipa Batholith (Fig. 2). The bulk volume of the LJI is estimated to be in the range of 16 to 24 km³ (Table 1) based on a minimum surface area of 800 km² and on an average thickness of 20 m.

The LJI crops out in the Río Chili and Río Yura valleys, which cut at least 400 m-deep down in the eastern and western basin of Arequipa (Fig. 3). It is also exposed to the SW of the Arequipa depression along the upper part of the Río Vitor valley, from where it overflowed and covered the Vitor Piedmont. There, it overlays deposits of the uppermost Moquegua Formation.

In the Río Chili canyon, the LJI compound cooling unit comprises several flow units, resting on a rugged basement paleotopography. These flow units show 0.5- to 3-m-thick sole layers (layers 1 and 2a) displaying either a fines-rich or a lithic-rich (fines depleted) facies. Upstream along the Río Chili and overlying the RCI at the Aguada Blanca dam, the uppermost of the two LJI flow units ≥ 80 m in thickness of the LJI (Figs. 2 and 3, Section C–D) yielded an ^{40}Ar – ^{39}Ar age of 4.88 ± 0.22 Ma (Table 1).

To the SW of the Arequipa basin near the oasis of Añas Huayco, located downstream the Río Chili valley (Figs. 2 and 3, Sections A–B and E–F), the LJI shows a 15-m-thick valley-ponded lithofacies. The ignimbrite also crops out on top of the Arequipa Batholith near La Joya, 40 km WSW of Arequipa (Figs. 2 and 3, Section A–B), where the deposit is only 5 m thick. This distal LJI yielded an ^{40}Ar – ^{39}Ar age of 4.87 ± 0.02 Ma (Table 1 and Fig. 2), which is almost identical to that obtained at the Aguada Blanca dam. The occurrence of the LJI on top of the Arequipa Batholith implies that the flows either ran

up the 350-m-high northern scarp of the Arequipa Batholith (at a distance of ≥ 20 km from the presumed source located in the area of the Chachani massif), or that the scarp formed after deposition of the LJI due to recent tectonic movements, which is, however, rather unlikely.

To the NE of the Arequipa depression, the LJI is overlain by Plio-Quaternary Chachani volcanoclastic deposits and lava flows (one lava flow was dated at 0.833 ± 0.06 Ma by Thouret et al., 2001). In turn, these deposits are overlain by the El Misti lava flows.

3.3. The Arequipa Airport Ignimbrite (AAI)

The AAI forms the uppermost filling of the Arequipa depression between the Río Yura and the Río Chili valleys at elevations ranging from 1700 to 2700 m asl. Unlike the LJI, the AAI is not exposed to the North of the Chachani volcanic complex (Figs. 2 and 3), although a 1-m-thick tephra fall, which is stratigraphically equivalent to the AAI, was found to the ENE of the Chachani complex. The AAI consists of a white unit overlain by a pink unit.

3.3.1. The AAI white unit

The white unit crops out in narrow valleys which drain the depression from North to South (Figs. 2 and 3). The ignimbrite is mined in quarries and is the main source of the white building stone of Arequipa. The white unit ranges from a few tens of meters to as much as 150 m in thickness where it fills the Quebrada Cuico, a paleo-valley tributary to the Río Chili SW of the basin. The white unit of the AAI was not observed in the Río Chili canyon, although yellowish pumice-rich flow deposits, which overlie the LJI and RCI in the upper Río Chili valley, occupy a similar stratigraphic position to the white unit of the AAI. These deposits may correspond to distal pyroclastic flows associated with the main body of the white ignimbrite. The minimum surface of the AAI white unit is about 400 km² (Figs. 2 and 3) and it is 40 m thick on average, giving a preserved volume estimate of 15–20 km³ (Table 1).

3.3.2. The AAI pink unit

The pink unit forms most of the flat surface of the Arequipa depression. The pink unit is thicker in the middle of the depression (Fig. 3), but thins out towards its WNW edge and towards its ESE margin, as shown at the exit of the Río Chili canyon (Fig. 3: Chilina, Sections C–D and E–F). There, the pink ignimbrite overlies 8-m-thick pumice- and ash-fall deposits, which rest above the LJI (Fig. 2). The pink unit is probably

more widespread than the white unit (ca. 600 km²) but its thickness ranges from only a few meters up to 50 m. Toward the south, in the Arequipa depression and near the Arequipa Batholith, the 50-m-thick pink unit overlies the LJI without any intercalated white unit (Fig. 3: Sections A–B and E–F) but shows intercalated sediments that are a few meters thick. Based on an average thickness of 8 m, the preserved deposit volume is about 5 km³. The pink unit yielded an ⁴⁰Ar–³⁹Ar age of 1.65 ± 0.04 Ma (Table 1).

The lack of a stratigraphic unconformity and the absence of sediment or a buried soil between the two units of the AAI suggest a short time interval between the emplacement of the white and pink units. However, Vatin-Pérignon et al. (1996) reported a fission track age of 2.42 ± 0.11 Ma on obsidian clasts from the top of the white ignimbrite just below the 1.65 Ma-old pink unit, an age that is close to the K–Ar age of 2.9 ± 0.1 Ma given by the same authors for the white ignimbrite in the Quebrada Cuico. Hence, the available ages suggest a longer time interval ranging between 0.75 Ma and 1.25 Ma that elapsed between the emplacement of the white and pink units. Such a large hiatus, however, is inconsistent with our field observations. We also note that the color of these ignimbrites may not be strictly restricted to flow units and that temperatures decreased with distance from the source. Thus a proximal unit may grade from white to pink with distance and cooling, making distinctions and correlations without geochemical analyses difficult. More precise ⁴⁰Ar–³⁹Ar ages on the white unit are needed to better constrain the age of the AAI (see Paquereau et al., submitted for publication). The AAI, whose extent is smaller than that of the LJI, fills the Arequipa depression with deposits ranging between 5 and 100 m in thickness (Figs. 2 and 3).

3.4. The Quaternary Yura Tuffs (YT) and the Capillune Formation tuffs

At the base of the western flank of the Chachani volcanic complex, a series of greyish non-welded pumice-flow deposits, termed Yura Tuffs (YT), are intercalated with reworked pyroclastic deposits. The YT have filled a depression between the Cerro Nocarani (a relatively old edifice in the northern Chachani complex) to the east and the scarps of the Jurassic ‘Yura Group’ to the west. In addition, they have flowed 50 km down the Río Yura valley towards the confluence of Río Vitor (Figs. 2 and 3, Section A–B). Based on an extent of 150 km² and an average thickness of 10 m, the preserved YT volume is ca.

1.5 km³ (Table 1). To the northwest of the Arequipa depression, near the town of Yura, the YT overlie the pink unit of the AAI (Figs. 2 and 3). One of the Yura pumice-flow deposits has been ⁴⁰Ar–³⁹Ar dated at 1.02 ± 0.09 Ma along the road to Juliaca on the west flank of the Chachani complex, 17 km north of the town of Yura (Table 1 and Figs. 1 and 2).

North and NE of Chachani on the Altiplano, lake sediments, tephra-fall deposits, as well as two beds of non-welded ash- and pumice-flow deposits (10 to 30 m thick) of the Capillune Formation crop out (Guevara, 1969). The ash- and pumice-flows were deposited on lake sediments which became deformed. The deformation features indicate a direction of displacement towards the ENE, which is consistent with a source located WSW, i.e. north of or below the Chachani complex. These ash- and pumice-flow and fall deposits may therefore be stratigraphically equivalent to the YT, as indicated by preliminary geochemical data.

In summary, the Arequipa area hosts deposits which record three large-volume Neogene ignimbrites but also small-volume tuffs of Quaternary age, which are intercalated with lava flows and volcanoclastic deposits from the stratovolcanoes in the area. The three major ignimbritic pulses produced the RCI ca. 13.07–13.39 Ma, the LJI ca. 4.78–4.89 Ma, and the AAI ca. 1.65 Ma. The YT and the Capillune ash- and pumice-flow and -fall deposits were produced by early Quaternary volcanoes or large vents in the northern area of the Chachani volcanic complex.

4. Lithofacies and degrees of welding

Our study of the lithofacies of the ignimbrites is based on petrographic features, macroscopic and microscopic observations, and on lithological components (Table 1). Lithofacies were described using the classification of Branney and Kokelaar (2002). Fig. 4 shows the facies variations displayed by the Arequipa Ignimbrites. All ignimbrites are vitric tuffs (after Schmid, 1981; Table 1), with 60 to 80 vol.% glass and pumice, 15 to 30 vol.% free crystals, and 5 to 25 vol.% lithic fragments.

We have used the schemes of Streck and Grunder (1995) and Quane and Russell (2005) to estimate welding degrees in Neogene ignimbrites. Eight ranks of welding have been recognized by these authors based on specific changes in macroscopic and/or microscopic textures, such as lapilli oblateness and fabric orientation (Fig. 4). Rank I is characterized by undeformed and randomly oriented pumice in an unconsolidated matrix of ash. In rank II the pumice remains randomly oriented

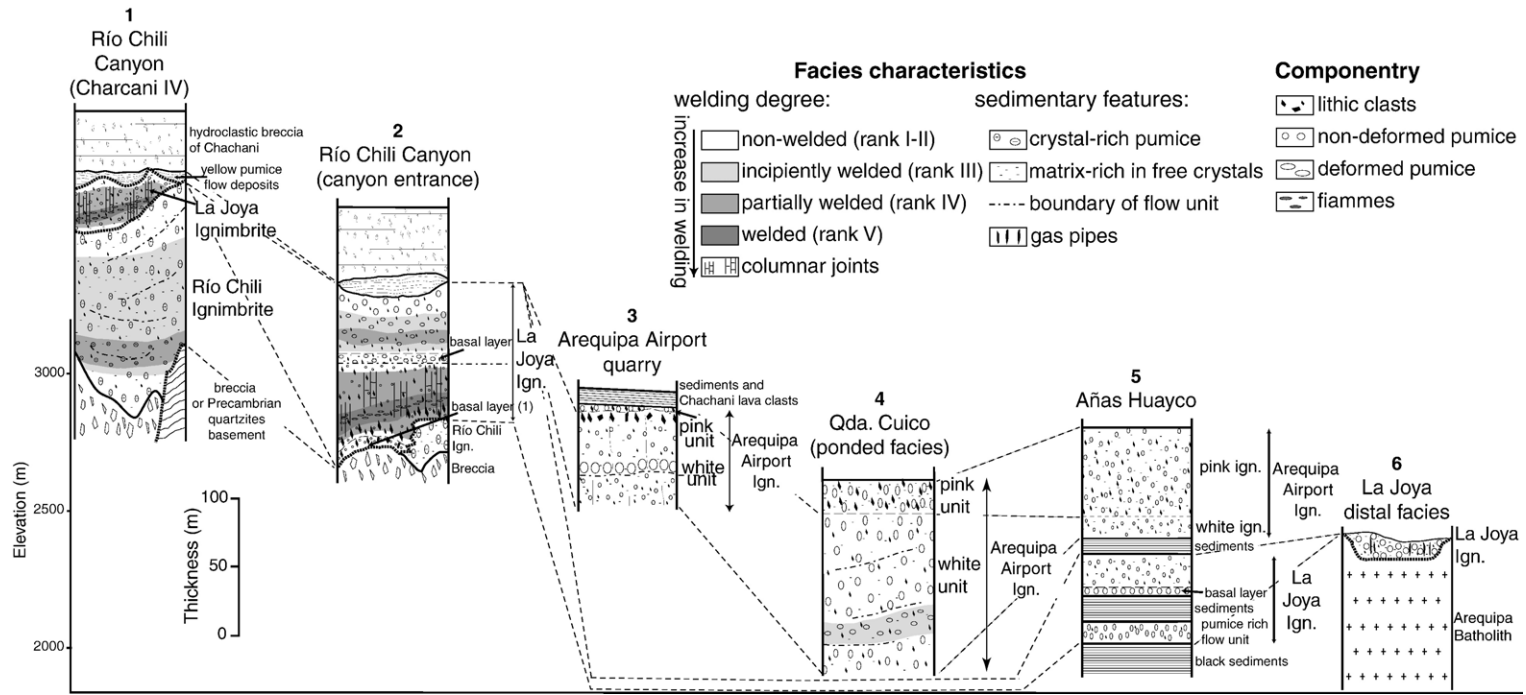


Fig. 4. Measured stratigraphic sections of the Neogene ignimbrites in the Arequipa depression and on top of the Arequipa Batholith. Location of sections is shown in Fig. 3.

but the deposit is now consolidated. By rank III the textural effects of welding are apparent, e.g. slight alignment of pumice lapilli, incipient deformation of bubbles and shards. In rank IV, glass shards are deformed around rigid inclusions, pumice lapilli are clearly flattened and define a pervasive foliation. Rank V rocks are eutaxitic at all scales. In rank VI pumice are fully collapsed to vitrophyric fiammes and have virtually no porosity. In rank VII samples appear as massive vitrophyre and rank VIII samples exhibit textures associated with rheomorphism.

4.1. The RCI: crystal-rich massive lapilli tuffs

The RCI contains a massive lapilli-tuff facies, rich in pumice blocks as large as 15 cm across with rounded vesicles and a high crystal content (Fig. 4, sections 1 and 2). The grey to pink matrix is rich in free crystals (30 vol.%), and displays a mineral assemblage similar to that of the pumice blocks. The mineral assemblage consists of plagioclase, sanidine, quartz, Fe–Ti oxides, and up to 15 vol.% biotite and amphibole (Table 1). The amphibole content may be used to distinguish the RCI, as this mineral appears only in trace amounts in all other Arequipa Ignimbrites.

Different facies within the RCI are always consolidated but pumice block textures vary from undeformed and randomly oriented at the top of the cooling unit to clearly flattened with a pervasive foliation toward the base. The RCI displays columnar jointing and strongly flattened and aligned pumices in the thickest deposit near Charcani IV (Fig. 3, Section C–D, and Fig. 4). This ignimbrite sheet displays a rank II to rank IV welding facies, i.e. consolidated with non-deformed pumices and shards to flattened pumices.

4.2. The LJI: welded lapilli tuffs

The LJI exhibits a large variation in degree of welding and lithofacies, from non-welded consolidated ignimbrites of rank I to partially welded ignimbrites of rank V (Fig. 4, sections 1, 2, 5, and 6). The common mineral assemblage includes plagioclase > quartz > sanidine > biotite > Fe–Ti oxide > amphibole. The LJI contains the highest contents of quartz and sanidine (15 vol.% and 25 vol.% of all minerals, respectively) amongst the Arequipa Ignimbrites.

In the Río Chili canyon (between Charcani I and II, Fig. 4, section 2), the LJI is thickest and shows a partially welded facies of rank V with fiamme structures and a devitrified matrix, i.e. the highest degree of welding of all Arequipa Ignimbrites. This thick and

welded facies reflects the most proximal facies observed for the LJI, and is also observed in the Río Sumbay valley (Fig. 2).

The medial to distal non-welded facies of LJI presents welding of rank I or II. In the southern part of the depression (near the oasis Añas Huayco; Fig. 4, section 5), the 10-m-thick deposit consists of a single, white, non-welded, flow unit rich in sanidine, plagioclase, quartz, and weathered biotite, and contains yellowish, weathered, undeformed pumices also rich in plagioclase and sanidine. A 1-m-thick basal layer is rich in cm-sized pumices identical to those of the overlying flow unit, e.g. yellowish and non-fibrous, but less weathered. The distal facies was observed near La Joya on the Arequipa Batholith, and on the Río Vitor piedmont (Fig. 4, section 6). There, the 5- to 10-m-thick deposit displays almost openwork pumice accumulations typical of distal regions of a flow. Exposures on the Río Vitor piedmont near the town of Vitor show many gas-escape pipes, which reflect interaction with a wet substrate during emplacement.

4.3. The AAI units: two ash and/or lapilli tuffs

The lithofacies of the two units of the AAI are shown in Fig. 4, sections 3, 4, and 5.

4.3.1. White unit: indurated massive ash-and-lapilli tuff

The white AAI sheet exhibits rank II welding, corresponding to an indurated facies without deformed pumice clasts and shards. Vapor-phase crystallization, a result of hot gas percolation throughout the deposit during the cooling process, has produced the induration of the ignimbrite after emplacement (Streck and Grunder, 1995; Barker, 1996) and the replacement, to varying degrees, of silicic glass by fine cristobalite and tridymite crystals with axiolitic texture. The textural effects of welding appear in the 150-m-thick cooling unit of the white ignimbrite in the SW part of the Arequipa depression (e.g., Quebrada Cuico, Figs. 2 and 4, section 4), where the intermediate and lowermost flow units display slightly aligned and deformed pumice and glass shards, in a dense grey matrix, corresponding to a rank III welding. The white to grey ashy matrix contains yellowish sandy pumices with rounded vesicles, accidental lava fragments, obsidian, and is rich in free crystals of plagioclase, weathered biotite, and sanidine.

The yellowish pumice-rich flow deposit, which is thought to be equivalent to the AAI white unit in the Río Chili canyon, is fines-depleted and contains two pumice

groups: weathered, pinkish fibrous pumice and small whitish, fresh pumice with spherical vesicles.

4.3.2. Pink unit: non-welded, massive, lithic-rich lapilli tuff

The pink unit matrix is richer in accidental lithic fragments (25 vol.%) than the white unit but with similar proportions: 42–60 vol.% of angular red to black andesite clasts, 7–22 vol.% obsidian fragments, and 24–34 vol.% of sedimentary rock clasts. Jenks and Goldish (1956) previously suggested that the andesite clasts, sometimes glassy, had probably been entrained from the vent area. The pink matrix also contains glass shards and fibrous white pumices, which are subaphyric (<10 vol.% crystals of plagioclase and biotite). The matrix also contains free crystals of plagioclase > biotite > Fe–Ti oxides, rare grey quartz and sanidine, and traces of amphibole. Thin sections reveal Fe–Ti oxide inclusions, mostly magnetite, in glass shards of the matrix and in crystals. Divided hematite is the origin of the pink color in the deposit (Fenner, 1948). The presence of quartz in the white unit of the AAI also distinguishes it from the quartz-free pink unit of the AAI.

The non-welded pink unit, which has undergone less recrystallization than the white unit, shows a rank I to II welding, i.e. a weakly lithified matrix with undeformed pumices (Fig. 4, sections 3, 4, and 5). Furthermore, the pink unit shows a massive facies without any vertical grain-size grading.

4.4. The YT, Capillune tuffs and tephra

The stratified ash and pumice-flow deposits are rich in pumice and glass shards (75–80 vol.%), and depleted in non-juvenile lithic fragments (5 vol.%). The ash matrix contains free crystals of plagioclase >> sanidine > biotite > Fe–Ti oxides and obsidian fragments. North and NE of the Chachani complex, the pumice and ash-flow deposits of the Capillune Formation display a lithofacies different from the YT. For example, we observed one flow rich in cm-sized pumices in a white ash matrix and another which consists of an ash-flow deposit without pumice and poor in crystals and lithic fragments.

5. Mineralogical and chemical correlations

Our stratigraphy and Ar–Ar dating results enable us to distinguish four ignimbrite sheets: the RCI, the LJI, the AAI, and the YT. In this section, we will present mineralogical and chemical similarities and differences amongst the Arequipa Ignimbrites.

5.1. Phenocryst mineralogy

The feldspar component consists of both plagioclase and alkali feldspar phenocrysts. All the Arequipa Ignimbrites contain sodic plagioclase phenocrysts (An₁₃ to An₄₅), which dominate the mineral assemblage. Alkali feldspars, more abundant in the LJI and the RCI, consist of sanidine with a narrow compositional range (Or₅₅–Or₆₅). Biotite phenocrysts occur in all Arequipa Ignimbrites and show wide variations in composition. However, biotites often show incipient to strong alteration that makes the interpretation of microprobe data difficult and limits the usefulness of this mineral for correlation and dating. Nevertheless, MnO and Al₂O₃ contents in fresh biotite can be used to distinguish the Arequipa Ignimbrites (Fig. 5A and Table 2). De Silva and Francis (1989) and Harangi et al. (2005) also successfully used Mn, Ti, and Mg contents in biotite in order to discriminate ignimbrite units in the Central Andes and Carpathian–Pannonian Region, respectively. On a MnO–Al₂O₃ variation diagram, LJI biotites are richer in MnO but poorer in Al₂O₃ than the other ignimbrites (Fig. 5A). The

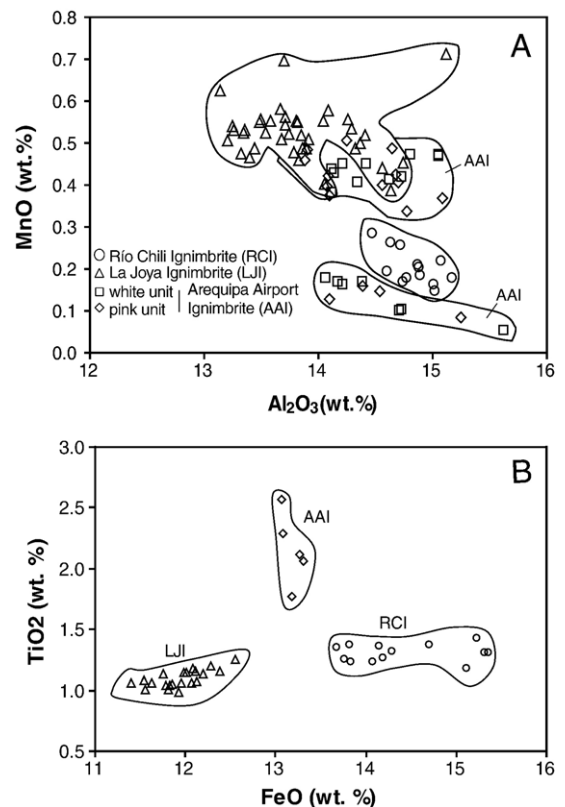


Fig. 5. Plots using analytical data of biotite (A) and amphibole (B) phenocrysts. Key for symbols is shown in the diagram caption.

Table 2
Electron microprobe analyses of amphiboles and biotites

	Pink unit of AAI					White unit of AAI						RCI
	71-amph1	71-amph3	71-amph4	71-biot5	71-amph5	48-amph1	79-amph1	79-amph2	79-amph3	79-amph4	79-amph6	18a-amph1
SiO ₂	45.40	43.18	44.49	43.66	46.59	48.20	43.81	44.03	44.07	43.86	43.43	45.93
TiO ₂	2.07	2.57	2.12	2.28	1.77	1.25	3.37	3.22	2.89	3.20	2.48	1.43
Al ₂ O ₃	9.63	11.83	10.99	11.65	8.43	8.28	10.60	10.62	10.52	10.59	10.51	8.73
FeO	13.31	13.07	13.26	13.09	13.18	13.47	11.80	11.71	12.10	12.09	14.09	15.23
MnO	0.07	0.04	0.05	0.05	0.09	0.51	0.05	0.04	0.05	0.05	0.05	0.53
MgO	14.27	13.65	14.11	13.75	14.73	14.90	14.65	14.83	14.80	14.55	13.96	14.26
CaO	11.81	12.34	11.68	12.17	11.93	11.46	12.15	12.16	12.07	12.10	11.99	11.74
Na ₂ O	2.17	2.29	2.28	2.32	1.90	1.37	2.56	2.50	2.55	2.56	2.42	1.46
K ₂ O	0.69	0.72	0.62	0.72	0.63	0.49	0.73	0.65	0.70	0.69	0.70	0.58
BaO	0.00	0.01	0.00	0.00	0.04	0.00	0.06	0.02	0.01	0.07	0.05	0.02
SrO	0.53	0.27	0.41	0.30	0.66	0.00	0.23	0.21	0.24	0.23	0.30	0.00
Cl	0.05	0.03	0.00	0.00	0.04	0.06	0.01	0.02	0.00	0.01	0.00	0.08

	RCI											
	18a-amph2	18a-amph3	18a-amph4	18a-amph5	18a-amph6	18a-amph10	18b-amph1	18b-amph2	18b-amph3	18b-amph4	18b-amph6	18b-amph7
SiO ₂	46.79	47.30	46.81	48.00	46.69	46.34	47.96	48.03	47.64	47.60	46.70	47.90
TiO ₂	1.32	1.26	1.37	1.25	1.36	1.31	1.18	1.23	1.37	1.36	1.31	1.23
Al ₂ O ₃	8.58	8.59	8.76	7.83	8.66	8.59	7.76	8.06	8.60	8.27	8.83	8.11
FeO	14.29	14.19	14.70	13.77	13.68	15.32	15.12	14.07	13.82	14.15	15.36	13.83
MnO	0.43	0.48	0.46	0.49	0.36	0.53	0.44	0.52	0.45	0.48	0.51	0.44
MgO	14.35	14.22	13.92	14.89	14.98	13.53	13.46	14.24	14.38	14.45	13.24	14.72
CaO	12.12	11.81	11.86	11.80	12.11	12.28	12.05	11.71	11.70	11.70	11.87	11.77
Na ₂ O	1.33	1.38	1.35	1.29	1.38	1.23	1.17	1.31	1.36	1.36	1.34	1.36
K ₂ O	0.71	0.61	0.66	0.56	0.67	0.74	0.75	0.72	0.57	0.51	0.77	0.54
BaO	0.00	0.05	0.00	0.05	0.01	0.04	0.01	0.00	0.03	0.05	0.00	0.02
SrO	0.00	0.00	0.00	0.00	0.03	0.01	0.00	0.00	0.00	0.00	0.00	0.00
Cl	0.07	0.08	0.06	0.06	0.06	0.08	0.08	0.08	0.07	0.07	0.08	0.06

	LJI										
	19-ampha	19-amph1	19-amph2	19-amph3	68-amph1	68-amph1a	68-amph1b	81-amph1	81-amph2	81-amph3	81-amph4
SiO ₂	50.78	51.47	50.42	50.50	51.70	51.50	50.32	50.61	51.03	50.74	51.29
TiO ₂	1.06	1.01	1.15	1.07	1.06	1.04	1.25	1.16	1.13	1.06	1.05
Al ₂ O ₃	4.88	4.59	5.08	5.14	4.93	4.83	5.68	5.32	5.03	5.09	4.87
FeO	12.07	11.55	11.98	12.13	11.39	11.78	12.56	12.11	11.75	11.95	11.86
MnO	1.03	1.09	1.08	1.02	2	1.10	0.85	0.86	0.90	1.04	1.07
MgO	16.47	16.79	16.43	16.31	16.39	16.24	15.38	15.97	16.24	16.39	16.33
CaO	11.71	11.62	11.68	11.76	11.49	11.51	11.56	11.71	11.58	11.55	11.40
Na ₂ O	1.42	1.36	1.49	1.42	1.40	1.44	1.65	1.51	1.62	1.47	1.50
K ₂ O	0.50	0.43	0.56	0.54	0.51	0.44	0.60	0.57	0.54	0.52	0.45
BaO	0.00	0.00	0.00	0.00	0.04	0.03	0.03	0.08	0.02	0.03	0.08
SrO	0.00	0.00	0.00	0.00	0.00	0.00	0.02	0.00	0.04	0.06	0.02
Cl	0.08	0.09	0.10	0.10	0.08	0.09	0.11	0.08	0.10	0.08	0.09

AAI's biotites display two different compositional groups. Their MnO contents do not correlate with analyses totals (i.e., low-MnO biotites do not necessarily correspond to low-total analyses), which means that low MnO contents are not directly associated to alteration processes (vapor-phase crys-

tallization). Moreover all samples from the white unit of AAI present the same vapor-phase crystallized facies. Thus, the two biotite populations in AAI may reflect the coexistence of phenocryst and xenocryst biotites in the whole-rock matrix. Exsolved Fe–Ti oxides (Ti-poor titanomagnetite and titanohematite)

Table 2 (continued)

	LJI									
	81-amph5	81-amph6	66-amph5	66-amph6	66-amph7	66b-amph1	21-amph-b	21-amph1	21-amph3	21-amph4
SiO ₂	51.36	51.65	50.35	51.49	50.49	50.65	49.91	50.10	50.71	50.98
TiO ₂	1.00	1.06	1.20	1.08	1.18	1.15	1.16	1.14	1.04	0.99
Al ₂ O ₃	4.84	4.51	5.42	4.72	5.34	5.32	5.21	5.10	4.67	4.75
FeO	11.81	11.62	12.29	11.55	12.08	12.01	12.39	12.20	11.83	11.93
MnO	1.08	1.10	1.07	1.05	0.89	0.99	1.08	0.95	1.16	1.06
MgO	16.31	16.76	16.00	16.48	15.88	16.21	16.33	16.42	16.64	16.58
CaO	11.59	11.30	11.42	11.61	11.94	11.42	11.81	11.95	12.04	11.77
Na ₂ O	1.44	1.48	1.63	1.44	1.47	1.52	1.47	1.47	1.33	1.37
K ₂ O	0.46	0.45	0.52	0.45	0.61	0.54	0.53	0.56	0.40	0.47
BaO	0.02	0.00	0.00	0.02	0.00	0.05	0.02	0.00	0.05	0.00
SrO	0.00	0.02	0.00	0.00	0.01	0.00	0.00	0.00	0.04	0.04
Cl	0.08	0.07	0.09	0.07	0.09	0.10	0.09	0.10	0.07	0.07

	Pink unit of AAI												
	16-biot1	16-biot8.2	42-biot1	42-biot2	42-biot3	42-biot4	42-biot5	71-biot1	71-biot2	71-biot4	73-biot1	73-biot3	73-biot4
SiO ₂	38.31	38.07	38.43	38.06	38.48	38.65	37.37	38.48	39.27	38.80	38.78	37.81	39.36
TiO ₂	4.60	4.58	4.69	4.48	4.33	4.42	4.81	4.80	4.58	4.65	4.57	4.45	4.71
Al ₂ O ₃	14.25	14.64	13.88	14.55	15.08	14.78	14.68	14.53	14.10	14.38	13.91	14.70	14.08
FeO	16.03	16.44	16.29	16.42	15.41	15.84	16.68	14.91	14.97	15.01	16.43	16.52	16.30
MnO	0.51	0.49	0.46	0.40	0.37	0.34	0.42	0.15	0.13	0.16	0.48	0.41	0.42
MgO	15.37	14.54	15.03	15.10	15.52	15.32	14.86	15.94	15.90	15.87	15.06	14.94	15.46
CaO	0.04	0.08	0.00	0.02	0.00	0.04	0.00	0.03	0.00	0.00	0.02	0.00	0.20
Na ₂ O	0.58	0.52	0.59	0.60	0.90	0.71	0.64	0.78	0.65	0.78	0.67	0.75	0.69
K ₂ O	9.28	9.23	9.64	9.19	8.74	8.89	9.40	9.26	9.35	9.27	9.09	9.29	7.91
BaO	0.83	1.17	0.81	1.01	1.04	0.89	1.04	0.91	0.79	0.80	0.71	1.03	0.70
SrO	0.00	0.00	0.00	0.00	0.00	0.00	0.00	0.21	0.24	0.27	0.19	0.12	0.16
Cl	0.20	0.19	0.17	0.17	0.10	0.11	0.10	0.00	0.03	0.00	0.10	0.00	0.00

	White unit of AAI											
	22-biot3	22-biot4	22-biot6	22-biot-a	43b-biot1	43b-biot4	43b-biot5	43b-biot6	43b-biot7	48-biot1	48-biot2	
SiO ₂	36.64	37.45	37.52	36.91	38.28	38.00	38.92	38.66	38.95	38.01	38.39	
TiO ₂	4.76	4.61	4.56	4.73	4.60	4.59	4.62	4.59	4.51	4.47	4.52	
Al ₂ O ₃	15.06	14.73	14.42	14.81	14.39	14.71	14.17	14.22	14.06	14.63	14.12	
FeO	17.58	16.78	16.78	17.00	16.31	16.17	15.87	15.97	15.88	16.49	16.46	
MnO	0.47	0.42	0.45	0.47	0.17	0.10	0.17	0.16	0.18	0.41	0.44	
MgO	14.18	14.93	15.09	14.97	14.67	14.84	15.00	14.75	14.89	14.85	14.96	
CaO	0.00	0.01	0.02	0.00	0.00	0.00	0.03	0.01	0.01	0.02	0.00	
Na ₂ O	0.67	0.68	0.65	0.69	0.61	0.69	0.61	0.70	0.69	0.76	0.75	
K ₂ O	9.45	9.30	9.29	9.20	9.59	9.58	9.52	9.65	9.56	9.29	9.18	
BaO	1.01	0.93	1.02	1.04	0.89	0.88	0.68	0.87	0.81	0.92	1.01	
SrO	0.00	0.00	0.00	0.00	0.49	0.43	0.41	0.41	0.46	0.05	0.00	
Cl	0.18	0.17	0.19	0.16	0.00	0.02	0.00	0.00	0.00	0.11	0.18	

occur as free crystals in the matrix and pumice, and as inclusions in plagioclase, biotite, and amphibole. Magnetic properties of the deposits indicate variation of the magnetic mineral assemblage, not detected by microscopic observations nor by microprobe analysis on large (>50µm) Fe–Ti oxide grains. For example, a vertical section in the thick white unit of the AAI

(Quebrada Añas Huayco, SW part of the Arequipa depression), shows changes in magnetic signatures (unblocking temperature, magnetic susceptibility) from titanohematite at the top of the unit to titanomagnetite at the base. Titanomagnetite signature has been observed in the uppermost pink unit of AAI and most of the LJI samples (Paquereau et al., submitted for publication).

Table 2 (continued)

	LJI											
	19- biot1	19- biot3	19- biot5	19b- biot1	19b- biot3	19b- biot4	19b- biot6	19b- biot7	19b- biot10	68- biot2	68- biot3	68- biot5
SiO ₂	38.41	38.37	36.64	37.65	38.32	38.09	38.81	38.39	37.91	38.43	38.47	38.70
TiO ₂	4.64	4.82	4.07	4.61	4.59	4.76	4.54	4.73	4.79	4.87	4.85	4.76
Al ₂ O ₃	13.86	13.71	13.07	14.53	14.05	14.56	14.64	13.82	14.41	13.91	13.82	13.84
FeO	16.42	16.14	22.17	18.60	16.46	17.63	16.72	16.25	16.64	15.85	15.96	15.71
MnO	0.49	0.56	0.82	0.82	0.40	0.44	0.39	0.46	0.52	0.51	0.55	0.52
MgO	15.15	15.26	13.51	13.50	15.08	14.17	14.19	15.32	14.65	15.30	15.17	15.42
CaO	0.00	0.07	0.04	0.03	0.00	0.00	0.06	0.03	0.02	0.05	0.00	0.00
Na ₂ O	0.60	0.57	0.55	0.46	0.62	0.58	0.57	0.75	0.64	0.60	0.58	0.59
K ₂ O	9.46	9.27	8.60	8.75	9.33	8.83	8.90	9.09	9.11	9.29	9.39	9.36
BaO	0.77	1.02	0.11	0.86	0.97	0.80	1.02	0.96	1.02	1.00	0.97	0.89
SrO	0.00	0.00	0.00	0.00	0.00	0.00	0.00	0.00	0.00	0.00	0.04	0.00
Cl	0.20	0.18	0.19	0.18	0.15	0.14	0.13	0.19	0.12	0.19	0.20	0.20

	LJI											
	34- biot1	34- biot2	66- biot5	66- biot7	66b- biot5	17a- biota	17a- biot9	17a- biotb	17b- biot5	21- biot7	21- biot-a	20- biot1
SiO ₂	39.83	38.65	39.03	40.56	39.36	39.68	41.61	38.75	39.75	38.62	36.53	39.80
TiO ₂	4.44	4.74	4.80	4.54	4.68	4.50	4.42	4.68	4.67	4.33	4.91	4.36
Al ₂ O ₃	13.34	14.04	13.74	13.25	13.48	13.32	13.40	13.54	13.44	13.14	14.26	13.70
FeO	15.81	16.04	16.32	15.73	16.00	15.46	14.72	16.04	15.40	16.64	17.28	16.19
MnO	0.53	0.55	0.52	0.54	0.55	0.48	0.47	0.53	0.49	0.62	0.56	0.70
MgO	15.72	15.19	15.12	15.61	15.51	16.01	15.10	15.55	15.72	15.95	14.92	14.99
CaO	0.00	0.00	0.07	0.05	0.01	0.05	0.08	0.01	0.11	0.05	0.02	0.09
Na ₂ O	0.38	0.50	0.68	0.48	0.47	0.54	0.56	0.54	0.54	0.61	0.62	0.49
K ₂ O	9.55	9.32	8.77	8.81	9.08	9.66	9.18	9.24	9.09	9.56	9.33	9.29
BaO	0.20	0.80	0.75	0.25	0.65	0.12	0.22	0.87	0.55	0.26	1.35	0.22
SrO	0.00	0.00	0.00	0.00	0.02	0.00	0.00	0.00	0.00	0.00	0.00	0.00
Cl	0.19	0.16	0.21	0.18	0.17	0.19	0.23	0.20	0.22	0.20	0.22	0.14

	RCI												
	18a- biot1	18a- biot2	18a- biot3	18a- biot4	18a- biot6	18a- biot7	18b- biot1	18b- biot2	18b- biot3	18b- biot4	18b- biot5	18b- biot6	18b- biot7
SiO ₂	38.07	38.13	37.90	38.02	38.48	37.92	38.74	38.86	38.59	38.11	38.40	38.89	38.57
TiO ₂	4.39	4.40	4.34	4.55	4.48	4.52	4.39	4.50	4.40	4.43	4.47	4.54	4.56
Al ₂ O ₃	14.47	14.63	14.72	15.18	14.88	14.89	15.02	15.08	14.74	14.60	14.87	15.01	14.77
FeO	18.62	18.25	18.43	15.81	15.82	15.63	15.01	14.77	15.27	17.25	16.55	15.15	15.58
MnO	0.28	0.26	0.26	0.18	0.20	0.19	0.15	0.22	0.17	0.19	0.21	0.16	0.18
MgO	13.66	13.81	13.62	15.62	15.49	15.63	16.03	15.97	16.24	14.42	14.82	15.71	15.67
CaO	0.00	0.05	0.10	0.05	0.03	0.01	0.03	0.01	0.03	0.00	0.00	0.05	0.02
Na ₂ O	0.37	0.38	0.40	0.37	0.48	0.50	0.58	0.57	0.53	0.50	0.50	0.49	0.55
K ₂ O	9.46	9.43	9.54	9.53	9.40	9.49	9.19	9.41	9.33	9.56	9.57	9.20	9.40
BaO	0.50	0.51	0.58	0.55	0.58	1.04	0.73	0.48	0.57	0.80	0.48	0.66	0.56
SrO	0.00	0.00	0.00	0.00	0.00	0.00	0.00	0.00	0.00	0.00	0.00	0.00	0.00

Data recalculated to 100% anhydrous. Minerals have been analysed using the JEOL LXA 89000R microprobe of Geochemie Institut at Göttingen University. Acceleration voltage: 15kV, current intensity: 2×10^{-8} A, and probe diameter: 10 μ m.

Because feldspars and Fe–Ti oxide crystals are generally altered, they display a wider range in composition within a single rock than between different ignimbrites. Hence, they are of no use for correlation purposes.

The most diagnostic results for distinguishing ignimbrite sheets in this region stem from the

composition of amphiboles. Amphiboles occur in the RCI (15 vol.% of crystal content), LJI (4 vol.%), and as traces in the pink unit of the AAI, and display significant compositional variations between ignimbrites. Most of the amphiboles are edenite (Na + K \gg 0.5). De Silva and Francis (1989) used Mn,

Fe, and Mg contents of amphiboles to fingerprint ignimbrites in the Central Andes but considered Al and Ti contents useless for correlation as they are not sufficiently different. Ti, Fe, Al, and Mn contents of amphiboles of the Arequipa Ignimbrites, however, gave the best correlation results. The LJI amphiboles are poor in TiO₂ (1.07–1.15 wt.%), FeO (11.85–12.09 wt.%) and Al₂O₃ (4.92–5.16 wt.%) and are MnO rich (0.98–1.06 wt.%) when compared to other compositions in other units (Fig. 5B and Table 2). Amphiboles of the pink unit of the AAI and the RCI show higher contents of TiO₂ (1.28–2.16 wt.%), FeO (13.85–14.45 wt.%), and Al₂O₃ (8.27–10.50 wt.%), which is consistent with the less differentiated compositions of the corresponding bulk rock (Table 3).

In summary, the petrographic features (i.e., occurrence or lack of certain minerals) together with the composition of phenocrysts, especially of amphiboles and biotites, can be applied as correlation tools in the case of the Arequipa Ignimbrites. Especially amphibole contents and compositions are significantly distinct in the LJI, the RCI and the pink unit of the AAI, and allow quick and efficient discrimination.

5.2. Pumice major element chemistry

Geochemical correlation should be based on juvenile pumice compositions, because the matrix or the ignimbrite bulk rock sample is subject to fractionation, mixing, and contamination by conduit walls and basement rocks during eruption and flow emplacement (Hildreth and Mahood, 1985). Samples were pooled from >5 to 20 individual pumice clasts (depending on size from >5 cm to <2 cm) assuring that pumices were unaltered, macroscopically homogeneous, and fully representative. Pumices were cleaned with a brush to remove any adhering ignimbrite matrix that could bias the composition. Pumice populations were always found to be uniform, only pumices from Yura Tuffs show some heterogeneity, which was accounted for by a relatively large sample.

37 samples were analysed at the Abt. Geochemie at Göttingen University: geochemical data are presented in Table 3. Samples were analysed for major elements and Nb, Zr, Y, Sr, Rb, Ga, Zn, Cu, Ni, Co, Cr, V, Ba, and Sc using X-ray fluorescence (XRF). Rare earth elements (REE) and Li, Mo, Cs, Cd, Hf, Ta, W, Pb, Th, and U contents were measured by inductively coupled plasma–mass spectrometry (ICP–MS).

Most ignimbrites are calc–alkaline, high-K (K₂O > 4 wt.%) rhyolites (SiO₂ > 70 wt.%: Le Maitre et al., 1989; Fig. 6), few are subalkaline, and some samples from the La Joya Ignimbrite even reach alkaline composition. The LJI exhibits the highest K₂O, the lowest CaO, and MgO contents (Table 3: up to 6.67 wt.% K₂O, down to 0.5 wt.% CaO, and 0.03 wt.% MgO) and high SiO₂ contents (Table 3: up to 76.60 wt.%).

5.3. Trace element chemistry and Sr isotopic compositions of pumices

N-MORB-normalized spider diagrams of the Arequipa Ignimbrites exhibit typical compositions of continental margin volcanic arc magmas (Fig. 7). They display strong enrichment in the large ion lithophile elements (LILE: Cs, Rb, Ba, K) relative to the High field strength elements (HFSE: Nb, Ta), a typical feature of subduction-zone trace-element distribution patterns. Incompatible trace elements are abundant in comparison to oceanic–arc related lavas. The RCI and the LJI display stronger enrichment in Cs (5–13 ppm), Rb (150–289 ppm), Th (13.10–33.59 ppm), and U (2.74–6.68 ppm), than in the AAI and in the YT (Cs: 1.4–5 ppm, Rb: 104–175 ppm, Th: 3–15.8 ppm, U: 0.47–3.65 ppm) (Table 3), as shown by their respective Cs/Y ratios (Fig. 8). In addition, the RCI and the LJI display a weak negative Ba anomaly, and a lower Ba/Th ratio than other ignimbrites (Figs. 7B and 8).

The Arequipa Ignimbrites show moderate total REE contents (55–140 ppm, Table 3), and fractionated chondrite-normalized REE patterns (Fig. 9), with high LREE concentrations (40 to 150 times chondritic abundances) and high LREE/HREE ratios ($L_{\text{AN}}/Y_{\text{bN}}=8\text{--}23$). These observations are consistent with continental margin subduction related rocks.

The Arequipa Ignimbrites show three different REE patterns. A majority of LJI and RCI samples exhibit LREE > 100 times chondritic abundances and negative Eu anomalies (Eu/Eu*, Fig. 9C). These ignimbrites contrast with the YT samples, which are less enriched in LREE (50–80 times chondrite abundance) and unique in showing a positive Eu anomaly (Fig. 9A). The AAI displays an intermediate pattern but a scattered LREE enrichment (60–130 times chondrite abundance, Fig. 9B). RCI and AAI share a weak negative Eu anomaly.

Conversely, the studied ignimbrites exhibit little if any HREE fractionation (Sm/Yb) and low Sr/Y ratios (Sm/Yb < 3.1, and Sr/Y < 16.7, Fig. 10A). Flat HREE patterns with Sm/Yb < 16.7 and Sr/Y < 3.1 clearly

Table 3
Chemical analyses of pumices in the Arequipa ignimbrites

Sample	YT						Pink unit of AAI									White unit of AAI			
	PIG-02-45b	PIG-02-58	PIG-02-64	PIG-02-59	PIG-02-60	PIG-03-106	PIG-00-16	PIG-00-42	PIG-02-71	PIG-02-72	PIG-02-73	PIG-02-92	PIG-02-53	PIG-02-132	PIG-03-115	PIG-00-22	PIG-02-43b	PIG-02-79	PIG-02-78
SiO ₂	76.0	76.1	75.2	74.6	74.4	76.1	75.2	73.7	74.9	75.1	75.2	74.6	74.8	74.6	74.8	74.2	74.8	74.9	75.8
TiO ₂	0.154	0.155	0.195	0.229	0.223	0.151	0.183	0.224	0.191	0.189	0.186	0.143	0.194	0.191	0.226	0.223	0.182	0.186	0.154
Al ₂ O ₃	13.3	13.3	13.6	13.9	13.8	13.3	13.8	13.9	13.8	13.7	13.6	14.2	13.9	13.7	13.7	14.0	13.7	13.8	13.3
FeO	0.95	0.81	1.20	1.33	1.42	0.74	1.07	1.53	1.09	1.06	1.08	1.00	1.20	1.16	1.29	1.39	0.94	1.09	0.92
MnO	0.080	0.058	0.080	0.084	0.089	0.059	0.070	0.080	0.077	0.074	0.075	0.087	0.087	0.072	0.078	0.078	0.060	0.078	0.076
MgO	0.17	0.16	0.23	0.30	0.44	0.22	0.27	0.46	0.24	0.21	0.25	0.27	0.32	0.29	0.44	0.32	0.23	0.30	0.20
CaO	0.75	0.82	0.97	1.08	1.28	0.93	1.07	1.46	1.00	1.01	0.98	1.19	1.01	0.99	1.32	1.22	0.69	1.07	1.08
Na ₂ O	3.93	3.19	3.83	4.06	3.13	3.06	4.10	4.43	4.36	4.30	4.25	3.40	3.97	3.96	3.46	4.50	4.07	3.99	4.07
K ₂ O	4.63	5.37	4.64	4.42	5.24	5.42	4.27	4.19	4.31	4.31	4.39	5.00	4.47	4.97	4.69	4.04	5.26	4.47	4.42
P ₂ O ₅	0.032	0.022	0.041	0.046	0.057	0.026	0.046	0.064	0.045	0.044	0.045	0.051	0.052	0.050	0.058	0.057	0.042	0.043	0.028
Rb	116	164	115	113	119	175	104	109	113	117	113	125	115	110	136	109	253	112	115
Sr	120	117	169	196	205	131	206	209	171	159	160	229	177	169	208	208	144	178	131
Y	13.0	15.0	15.0	16.0	16.0	14.0	14.0	14.0	14.0	13.0	15.0	13.0	16.0	14.0	12.0	14.0	15.0	14.0	12.0
Zr	81	93	95	123	69	102	76	76	69	70	67	72	84	99	83	67	87	70	63
Nb	10.0	13.0	11.0	12.0	12.0	12.0	13.0	11.0	13.0	12.0	14.0	14.0	10.0	13.0	12.0	12.0	10.0	12.0	14.0
Cs	1.87	5.73	1.89	1.70	1.98	6.30	1.49	1.50	1.42	1.71	1.49	3.05	1.90	1.71	1.87	1.46	4.58	1.72	2.01
Ba	1122	884	1175	1087	1003	973	1239	1121	1164	1127	1148	1135	1144	1117	1231	1168	1007	1178	1069
Hf	2.89	3.23	3.15	3.82	2.40	3.85	3.20	2.76	2.58	2.65	2.53	2.73	2.93	3.65	3.08	2.56	3.04	2.65	2.46
Pb	25.42	10.70	17.67	23.12	25.29	10.30	20.39	23.66	16.12	21.22	20.22	26.62	24.31	19.10	19.20	29.98	22.64	20.56	22.15
Th	5.73	9.88	4.98	3.01	3.21	15.80	8.64	4.52	6.67	7.53	6.84	5.85	3.73	6.33	6.46	4.63	6.44	6.74	4.21
U	0.93	2.13	0.69	0.52	0.60	3.65	1.10	0.56	0.84	1.00	0.90	1.10	0.57	0.81	0.80	0.58	0.93	0.84	0.47
Ta	0.52	0.68	0.59	0.51	0.44	0.86	1.05	0.96	0.95	1.08	1.00	0.69	0.48	0.54	0.63	0.78	0.55	1.06	0.89
La	14.75	10.15	15.57	9.06	11.82	18.00	31.72	18.12	28.09	29.38	26.73	11.06	14.72	23.50	21.70	20.68	18.66	28.30	13.45
Ce	35.58	29.48	44.58	38.42	31.41	41.60	67.50	47.39	56.75	59.00	54.95	35.47	41.55	57.30	53.70	50.78	40.76	58.54	36.84
Pr	3.22	2.04	3.14	2.05	2.34	3.71	6.30	3.60	5.43	5.81	5.28	2.72	2.93	5.06	4.56	3.93	4.03	5.35	2.74
Nd	10.48	6.39	10.20	6.79	7.53	11.90	21.21	12.20	18.03	19.17	17.52	9.57	9.47	17.00	15.20	13.43	13.49	17.67	9.43
Sm	1.97	1.25	1.90	1.46	1.48	1.97	3.16	1.88	2.58	2.76	2.59	1.72	1.74	2.73	2.48	1.92	2.43	2.60	1.53
Eu	0.71	0.55	0.76	0.69	0.64	0.44	0.68	0.45	0.57	0.59	0.57	0.39	0.72	0.57	0.53	0.47	0.78	0.55	0.34
Gd	1.78	1.18	1.78	1.38	1.42	1.88	2.40	1.45	1.90	2.06	1.98	1.26	1.65	2.49	2.30	1.56	2.26	1.96	1.19
Tb	0.27	0.19	0.27	0.23	0.22	0.24	0.33	0.21	0.27	0.30	0.29	0.23	0.24	0.31	0.29	0.22	0.31	0.28	0.19
Dy	1.24	0.85	1.18	1.08	1.05	1.42	1.85	1.18	1.55	1.70	1.63	1.38	1.11	1.72	1.65	1.25	1.41	1.57	1.07
Ho	0.27	0.21	0.27	0.25	0.25	0.29	0.37	0.24	0.29	0.32	0.29	0.26	0.25	0.34	0.33	0.24	0.31	0.29	0.21
Er	0.77	0.58	0.79	0.71	0.69	0.93	1.06	0.71	0.88	0.92	0.93	0.83	0.71	1.05	1.00	0.71	0.86	0.88	0.65
Tm	0.16	0.13	0.16	0.14	0.15	0.15	0.16	0.11	0.13	0.15	0.13	0.13	0.14	0.16	0.16	0.11	0.17	0.13	0.10
Yb	0.90	0.72	0.87	0.82	0.83	1.01	1.09	0.71	0.83	0.94	0.87	0.85	0.79	1.08	1.03	0.71	0.94	0.89	0.68
Lu	0.17	0.15	0.17	0.16	0.15	0.17	0.17	0.12	0.14	0.15	0.14	0.13	0.15	0.17	0.16	0.11	0.17	0.14	0.11
Eu/Eu*	1.17	1.39	1.26	1.48	1.35	0.69	0.75	0.83	0.79	0.76	0.77	0.81	1.30	0.66	0.68	0.83	1.01	0.74	0.77
⁸⁷ Sr/ ⁸⁶ Sr							0.7081	0.7094								0.70872			0.70903
Error							0.000011	0.000009								0.00001			0.00001

Major elements and Nb, Zr, Y, Sr, Rb, Ba were analysed using XRF (Geochemie Institut at Göttingen University). Rare Earth elements (REE) and Cs, Hf, Ta, Pb, Th, U contents were measured by ICP-MS (Geochemie Institut at Göttingen University). Major elements are recalculated to 100% anhydrous.

Sample	White unit of AAI	LJI															RCI	
	PIG-03-130	PIG-00-19b	PIG-00-17a	PIG-00-17b	PIG-00-34	PIG-02-81	PIG-02-75	PIG-02-77	PIG-00-20	PIG-00-21	PIG-02-66bis	PIG-02-68	PIG-02-76	PIG-03-98	PIG-03-118b	PIG-03-101	PIG-03-131	PIG-00-18b
SiO ₂	74.7	75.3	75.5	75.2	75.8	76.1	76.0	75.6	74.9	73.0	76.2	75.7	76.4	76.6	74.5	75.0	76.7	72.9
TiO ₂	0.221	0.170	0.169	0.172	0.151	0.156	0.155	0.159	0.153	0.267	0.146	0.153	0.159	0.152	0.175	0.160	0.163	0.224
Al ₂ O ₃	13.7	13.7	13.7	13.9	12.9	13.0	13.1	13.5	14.2	13.8	13.0	13.0	12.7	12.7	14.4	14.4	13.6	14.6
FeO	1.52	1.04	1.05	1.07	0.91	0.85	0.91	0.89	0.90	2.11	0.88	0.93	0.91	0.90	1.10	1.00	0.44	1.54
MnO	0.076	0.030	0.081	0.064	0.055	0.049	0.059	0.083	0.058	0.094	0.061	0.062	0.055	0.034	0.070	0.058	0.024	0.044
MgO	0.63	0.11	0.51	0.55	0.14	0.18	0.13	0.49	0.21	0.39	0.10	0.13	0.13	0.12	1.22	0.17	0.03	0.27
CaO	1.37	0.70	0.72	0.73	0.78	0.78	0.68	0.69	0.66	1.27	0.61	0.90	0.70	0.53	1.12	0.74	0.49	1.06
Na ₂ O	2.53	4.05	2.80	2.76	4.34	3.30	3.76	3.10	2.22	4.21	3.46	3.78	3.19	2.98	2.78	3.20	3.69	4.64
K ₂ O	5.22	4.82	5.52	5.61	4.85	5.57	5.12	5.46	6.67	4.82	5.52	5.36	5.67	5.97	4.60	5.30	4.87	4.62
P ₂ O ₅	0.063	0.013	0.018	0.017	0.024	0.023	0.024	0.040	0.025	0.054	0.019	0.022	0.028	0.025	0.049	0.013	0.030	0.048
Rb	128	201	200	202	206	234	223	191	204	200	242	209	210	289	150	199	213	199
Sr	217	96	66	75	82	72	80	34	47	161	71	76	62	55	139	79	66	208
Y	13.0	16.0	19.0	18.0	16.0	18.0	14.0	16.0	20.0	17.0	17.0	15.0	15.0	17.0	15.0	20.0	16.0	18.0
Zr	80	62	76	86	73	64	66	84	86	77	83	81	80	90	106	99	90	81
Nb	12.0	12.0	15.0	14.0	12.0	11.0	13.0	15.0	16.0	14.0	13.0	14.0	13.0	13.0	11.0	15.0	12.0	10.0
Cs	1.78	6.45	11.43	14.03	10.58	11.26	13.00	5.93	6.61	3.57	13.03	10.39	11.20	19.10	6.50	10.80	6.17	7.93
Ba	980	731	441	502	502	452	591	317	390	706	519	520	469	379	759	634	483	1025
Hf	2.78	2.78	3.51	3.58	3.08	2.82	2.87	3.35	3.58	3.06	3.28	3.21	3.34	3.68	3.97	4.07	3.98	3.27
Pb	19	15.61	21.10	19.54	12.98	14.98	17.24	25.94	19.54	17.64	27.13	11.11	14.30	15.30	17.30	23.50	13.90	15.41
Th	7.27	27.11	33.59	17.55	25.68	25.19	25.90	15.31	17.55	21.24	20.01	18.34	26.10	27.10	13.10	21.80	29.50	20.82
U	0.829	4.50	6.68	4.25	6.08	5.51	6.23	3.76	4.25	3.59	5.04	4.05	7.13	8.02	2.74	6.45	7.34	3.99
Ta	0.632	1.08	1.57	1.24	1.47	1.04	1.10	1.68	1.24	1.30	0.61	0.80	0.49	0.63	0.83	0.62	0.57	1.07
La	24.5	28.91	36.36	25.43	24.17	25.62	28.64	22.98	25.43	28.87	15.68	12.51	24.60	20.40	23.00	15.60	36.10	27.17
Ce	56.8	57.02	77.48	57.55	51.89	52.67	55.38	48.85	57.55	60.01	33.81	31.23	49.90	43.90	55.10	32.10	58.70	58.77
Pr	4.97	5.14	6.95	5.43	4.67	4.93	5.24	4.87	5.43	5.36	3.22	2.54	5.00	4.41	4.28	3.44	6.95	5.03
Nd	16.2	16.10	21.72	18.59	14.93	15.35	16.70	16.66	18.59	17.76	10.35	8.20	15.60	14.20	13.70	11.20	21.60	16.21
Sm	2.64	2.37	3.21	3.01	2.16	2.25	2.34	2.68	3.01	2.68	1.78	1.42	2.34	2.36	2.16	1.83	3.25	2.41
Eu	0.542	0.47	0.45	0.47	0.35	0.34	0.35	0.38	0.47	0.55	0.45	0.38	0.31	0.26	0.45	0.29	0.48	0.56
Gd	2.5	1.93	2.55	2.28	1.66	1.73	1.80	1.99	2.28	2.09	1.69	1.42	2.19	2.29	2.09	1.77	3.10	1.86
Tb	0.313	0.26	0.37	0.35	0.25	0.26	0.26	0.32	0.35	0.31	0.24	0.22	0.27	0.30	0.26	0.24	0.39	0.25
Dy	1.77	1.45	2.12	2.01	1.53	1.57	1.50	1.80	2.01	1.80	1.07	0.96	1.53	1.79	1.51	1.42	2.18	1.44
Ho	0.35	0.30	0.44	0.39	0.31	0.31	0.30	0.34	0.39	0.36	0.25	0.23	0.31	0.36	0.31	0.29	0.42	0.29
Er	1.08	0.93	1.35	1.16	0.96	0.97	0.92	1.02	1.16	1.07	0.73	0.67	0.96	1.14	0.96	0.93	1.25	0.87
Tm	0.161	0.14	0.21	0.18	0.15	0.16	0.15	0.15	0.18	0.16	0.15	0.14	0.15	0.18	0.15	0.14	0.19	0.13
Yb	1.08	1.00	1.48	1.18	1.03	1.09	1.02	1.04	1.18	1.09	0.83	0.81	1.04	1.22	1.06	1.00	1.31	0.90
Lu	0.174	0.16	0.24	0.18	0.17	0.17	0.17	0.15	0.18	0.18	0.17	0.16	0.17	0.20	0.18	0.16	0.21	0.15
Eu/Eu*	0.64	0.67	0.48	0.55	0.57	0.53	0.52	0.50	0.55	0.71	0.78	0.81	0.42	0.34	0.65	0.49	0.46	0.81
⁸⁷ Sr/ ⁸⁶ Sr	0.70936	0.707289		0.707747	0.707535				0.707181		0.707531		0.707531		0.708953	0.707484	0.707545	
Error	8E-06	0.00001		0.000008	0.000007				0.000009		0.000011		0.000011		0.00001	0.000011	0.00001	

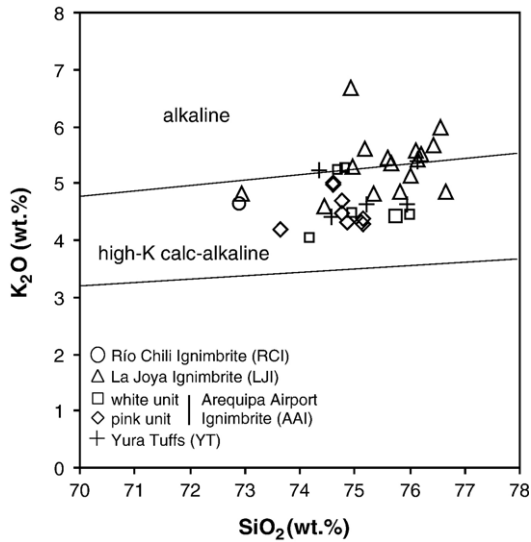


Fig. 6. Plot of K_2O vs. SiO_2 for bulk pumices. Compositional subdivisions after Le Maître et al. (1989).

exclude any significant role of garnet in the evolution of these ignimbrite magmas. Such limited HREE fractionation is, however, consistent with equilibration with a residual mineral assemblage containing pyroxene and amphibole, thus reflecting a differentiation at intermediate to shallow crustal levels (<40 km; [Mahlburg Kay and Mpodozis, 2002](#)). Given the “crustal” signatures in Sr, and Nd isotopes, we argue below that these magmas are partially derived from the crust, with some input of heat and melt from magmas that were derived from the mantle wedge of the subduction zone.

The Ba/Th ratio vs. Eu anomaly plot ([Fig. 10B](#)) displays three compositional groups: LJI and RCI have the lowest Ba/Th ratio associated with the largest negative Eu anomaly, typically reflecting a fractionation process controlled by sanidine. In contrast, most AAI pumices display a weaker negative Eu anomaly and a higher Ba/Th ratio, possibly indicating less sanidine fractionation. The YT trace elements show a larger scattering of Ba/Th ratios and positive Eu anomalies. In the Ba/Th vs. Rb/Sr diagram ([Fig. 10C](#)), the low Ba/Th ratios of the LJI and high Rb/Sr, contrast with those of the AAI and YT.

Sr isotopic compositions of AAI are higher than that in LJI ([Table 3](#) and [Fig. 11](#)). $^{87}Sr/^{86}Sr$ ratios in LJI vary from 0.70718 to 0.70810, and in AAI they range from 0.70872 to 0.70935.

The geochemical and mineralogical variations detected in the Arequipa Ignimbrites may be the

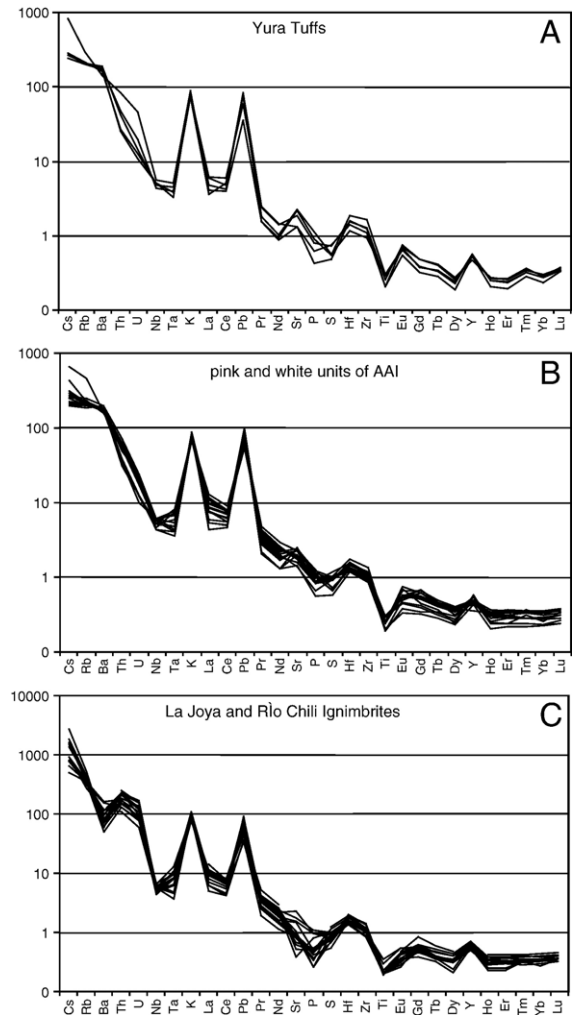


Fig. 7. N-MORB normalized multi-element variation diagram for pumice clasts of the four main ignimbrite sheets. Normalizing factors taken from [Sun and McDonough \(1989\)](#).

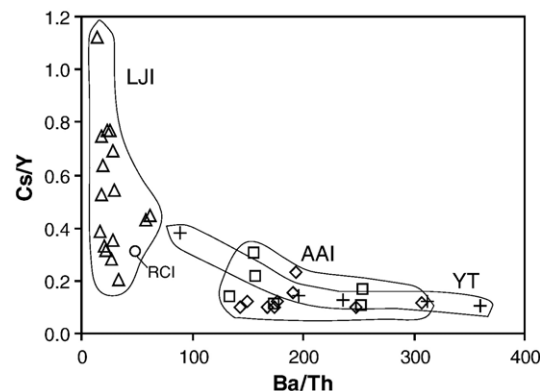


Fig. 8. Cs/Y vs. Ba/Th plot for the Arequipa area ignimbrites. Symbols as in [Fig. 6](#).

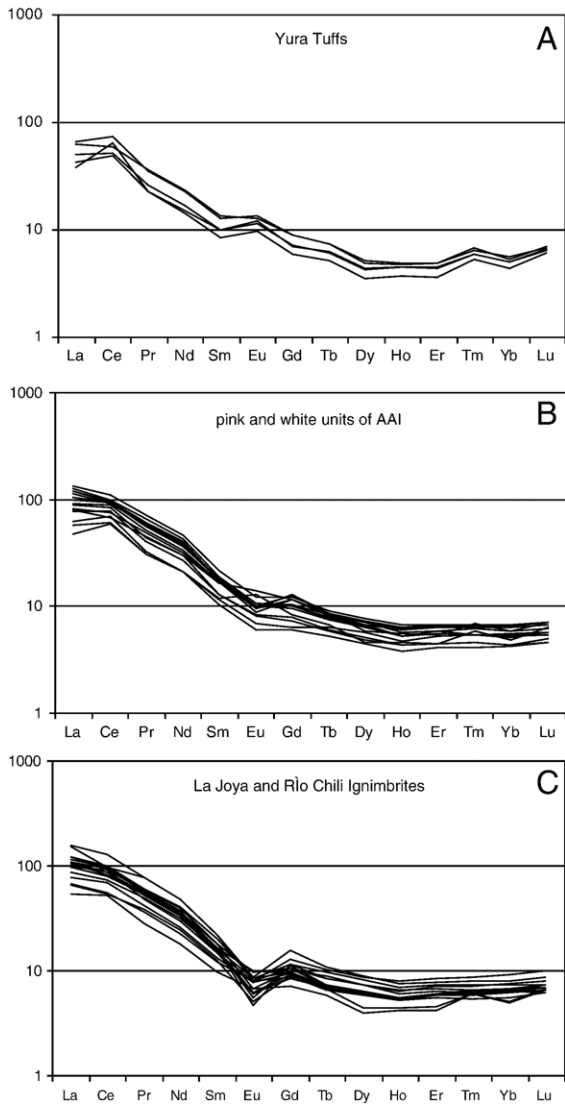


Fig. 9. Chondrite (C1)-normalized REE abundances for samples from four main ignimbrite sheets. Normalizing factors taken from Sun and McDonough (1989).

consequence of heterogeneities in the composition of the magma sources and/or in the variable degree of magmatic differentiation and crustal assimilation with time.

6. Discussion

Firstly, we discuss the use of geochemical compositions for the purpose of correlation. Secondly, the magmatic periods recorded by at least three voluminous ignimbrites are considered in the light of the uplift and erosion history of the Central Andes in southern Peru in order to determine how the

pyroclastic deposits have been sourced, erupted, and emplaced. Finally, we address the problem of vent locations.

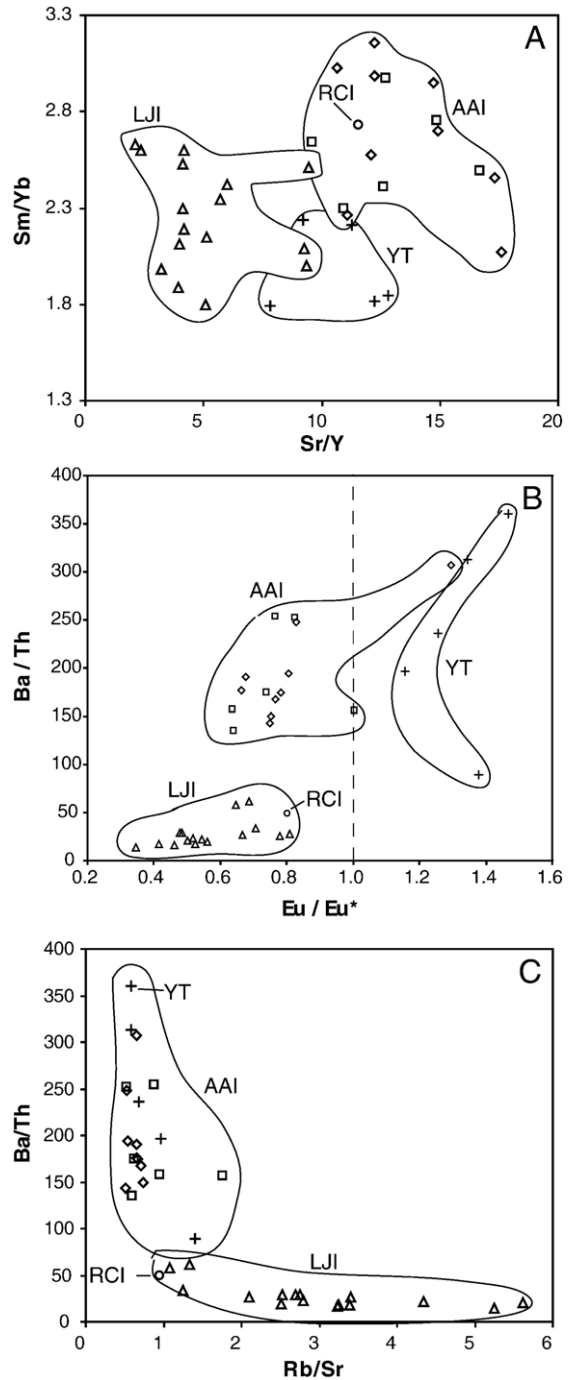


Fig. 10. Trace element ratio plots for the Arequipa Ignimbrites. (A) Sm/Yb vs. Sr/Y, (B) Ba/Th vs. Eu/Eu*, and (C) Ba/Th vs. Rb/Sr. Symbols as in Fig. 6.

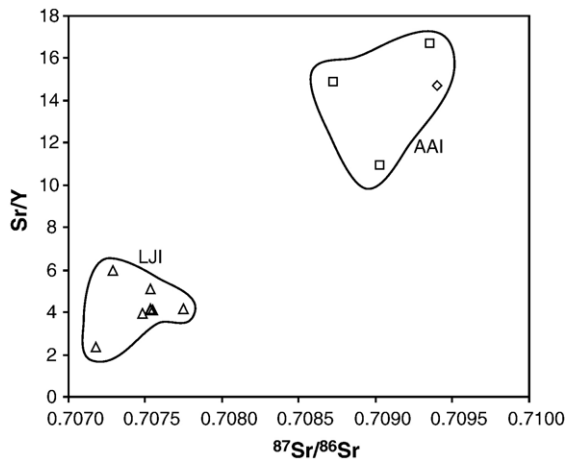


Fig. 11. Sr isotopic composition versus Sr/Y for the Arequipa Ignimbrites. Symbols as in Fig. 6.

6.1. Trace element and Sr isotope signatures

Trace elements and mineralogical data display compositional groups, which correlate with stratigraphic units and ages (Figs. 5, 10, and 11). As shown in Section 6.2, these four compositionally and stratigraphically different ignimbrites were emplaced during periods of high rates of convergence of the Nazca plate with respect to the South American plate.

Two compositional groups of ignimbrites and tuffs can be distinguished using major elements, REE, incompatible trace element ratios, and Sr isotopic ratios (Figs. 7–11, and Table 3). The first group consists of the Miocene RCI and Pliocene LJI, for whose differing amphibole chemistry is helpful in distinguishing them. As shown in Section 5.3, the LJI is more evolved than the other ignimbrites in terms of major and incompatible elements (e.g. high SiO₂, K₂O, and low CaO and MgO, enrichment in Cs, Rb, Th, U, and the LREE, and negative Ba and Eu/Eu* anomalies). However, the LJI also has lower Sr isotopic ratios, which suggest that it has suffered less crustal assimilation compared to the AAI. The second group comprises the younger AAI and YT. Positive Eu-anomalies in the YT help to distinguish it from the AAI. These two ignimbrites are less evolved than the LJI and RCI (less enriched in LILE and LREE, weaker or no Eu/Eu* and no negative Ba anomaly).

Thus, it is inferred that varying degrees of magmatic differentiation and crustal contamination were responsible for the observed compositional shifts between the two groups of ignimbrites. The less evolved younger ignimbrites (AAI and YT) were affected by larger

degrees of crustal contamination. Hildreth and Moorbath (1988), Walker et al. (1991), and Trumbull et al. (1999) have demonstrated that younger andesite/dacite arc lavas in the Chilean Andes display higher Sr isotopic ratios than older lavas. Alternatively, the shift in composition could be explained by different source proportions (mantle vs. crust) rather than by magmatic evolution. LJI and RCI initial melts are closer to the eutectic and are rather wet. With increasing time and more extensive melting of the crust, the AAI and YT initial melts are slightly less evolved and drier than RCI and LJI “granitic” initial melts. These drier melts would also have a higher temperature which would allow them to assimilate more crustal material as shown by their higher ⁸⁷Sr/⁸⁶Sr ratios.

Interpretations from refraction and broadband seismic data suggest that the crustal root is 70–74 km thick beneath the Western Cordillera (see reviews in Zandt et al., 1996; Gregory-Wodzicki, 2000). Many Quaternary magmas having traversed thick Andean crust show the geochemical fingerprint of garnet (HREE fractionation expressed as high Sm/Yb > 6 and Sr/Y > 40) either from a residual crustal assemblage during assimilation or from garnet fractionation at high pressures (> 40 km; Mahlborg Kay and Mpodozis, 2002; Mamani et al., 2004; Wörner et al., 2004; Thoutret et al., 2005). However, the flat HREE of the Arequipa Ignimbrites (Figs. 9 and 10a) are different from those of most modern Central Andean magmas, suggesting no role of garnet in their evolution. Thus, the low Sm/Yb ratios associated to high ⁸⁷Sr/⁸⁶Sr ratios are attributed to crustal melting and assimilation in the shallow level of the crust (Fig. 11).

6.2. Ignimbritic magmatism and uplift of the Western Cordillera

Table 4 shows relationships between uplift, tectonic phases, and ignimbrite episodes in southern Peru. Tosdal et al. (1984) suggest that the landforms of the western slopes of the Western Cordillera reflect episodic epeirogenic uplift (3 major stages, Table 4) of the Central Andes in response to compressional tectonic events, subsequent to the upper Eocene Incaic tectonic episode (ca. 42 Ma). Sébrier and Soler (1991) suggest that Andean uplift mainly occurred during Miocene times through discontinuous pulses that are roughly coeval with four discrete compressional episodes (Table 4). (1) The first uplift produced the lower Miocene Altos de Camilaca surface (S1 stage of Sébrier et al., 1988), which was mantled by the Alpabamba and Huaylillas ignimbrites. This uplift postdates the Aymara tectonic

Table 4
Relationships between ignimbritic volcanism, tectonic phases and uplift in southern Peru

Ages (Ma)	Neogene ignimbritic events in the Arequipa area	Neogene ignimbritic events in southern Peru	Tectonic events		Ages (Ma)
			Tectonic pulses	Uplift episodes	
0		Pleistocene Ignimbrites (ca. 1.6 – 0.4 Ma; Vatin-Perignon et al., 1996)		S3 uplift (Pleistocene, Sébrier et al., 1988)	0
1	YT			Valley and terrace stage	1
2	AAI		(ca. 2 Ma, Sébrier et al., 1988; Sébrier and Soler, 1991)	(early Pleistocene, Tosdal et al., 1984)	2
3		Sencca Ignimbrites (Lefevre, 1979; Vatin-Perignon et al., 1996; Thouret et al., 2004)			3
4	LJI				4
5					5
6			Quechua III (ca. 7 Ma, Sébrier et al., 1988; Sébrier and Soler, 1991; Mercier et al., 1992)	S2 uplift (late Miocene, Sébrier et al., 1988)	6
7					7
8					8
9		Chuntacala Formation (Tosdal et al., 1984; Sébrier et al., 1988)			9
10		Caraveli Ignimbrites (Thouret et al., 2004)	Quechua II (ca. 10 Ma, Sébrier et al., 1988; Sébrier and Soler, 1991)		10
11					11
12				14–10 Ma: Pampa Lagunas Apron Pediment (Tosdal et al., 1984)	12
13	RCI (Thouret et al., 2001)				13
14		Huaylillas Formation (Tosdal et al., 1984; Thouret et al., 2004)			14
15			Quechua I (ca. 15–17 Ma, Sébrier et al., 1988; Sébrier and Soler, 1991)		15
16					16
17					17
18		Alpabamba Formation (Thouret et al., 2004)			18
19		Tacaza group (Lefèvre, 1979)			19
≥ 20		“Nazca” and “Carumas” ignimbrites (24–22 Ma, Thouret et al., 2004)	Aymara tectonic stage (ca. 26–28 Ma, Sébrier et al., 1988)	≤ 25 Ma: Altos de Camilaca surface (Tosdal et al., 1984) S1 uplift (lower Miocene, Sébrier et al., 1988)	≥ 20

Continuous deformation that migrates eastward (Sempere et al., 1997)

Continuous uplift (Thouret et al., 2004)

stage (Sébrier et al., 1988; Sébrier and Soler, 1991; Gregory-Wodzicki, 2000; Kennan, 2000) as a late Oligocene (ca. 26Ma) tectonic episode of regional extent. The Aymara tectonic stage marks the beginning of fast Miocene Andean convergence. (2) The early to late Miocene succession of tectonic phases (Quechua I, II, III: Sébrier et al., 1988; Sébrier and Soler, 1991, Mercier et al., 1992) were accompanied by the widespread eruption of the ca. 10Ma Chuntacala ignimbrites (Tosdal et al., 1984). This active tectonic period generated the formation of multiple pediments associated with stages of uplift (Pampa Lagunas Apron Pediment: Tosdal et al., 1984; S2 stage, Sébrier et al., 1988). (3) Finally, Tosdal et al. (1984) and Sébrier et al. (1988), describe a Pleistocene uplift stage, not clearly associated with a tectonic phase.

By contrast, Semperé et al. (1997), Gregory-Wodzicki (2000), and Kennan (2000) suggest that deformation took place fairly continuously, and migrated eastward after the Incaic tectonic event. Based on valleys cutting and infilling history, Thouret et al. (2004) support the hypothesis of a continuous uplift of the Western Cordillera during the period between 14Ma and 4–6Ma (deep canyon of southern Peru cut the 16–14Ma Huaylillas Formation and are filled by 4–6Ma ignimbrites; Table 4), followed by declining uplift thereafter.

The intensity of magmatic activity has been linked to variations in the rate of plate convergence (Sébrier and Soler, 1991; Babeyko and Sobolev, 2005; Sobolev and Babeyko, 2005). Calc–alkaline magmatism reached a maximum in southern Peru during the period 26Ma to the Present, i.e., contemporaneously with the period of highest convergence, and quite independent of the state of stress of the region (Sébrier and Soler, 1991; Vatin-Pérignon et al., 1996). Peaks of ignimbritic activity are intercalated between major uplift phases and associated tectonic compressive pulses (Tosdal et al., 1984; Sébrier et al., 1988). The Neogene ignimbrites of the Arequipa area are well separated in time, dated at ~13.3Ma, ~4.8Ma, and ~1.6Ma, and ~1Ma, and are contemporaneous with the continuous period of Miocene and Pliocene uplift described by Thouret et al. (2004). These Arequipa Ignimbrites may coincide with three of the ignimbritic episodes recognized in southern Peru (Table 4). Four post-Eocene pulses of explosive volcanism are recognized in southern Peru, northwestern Bolivia, and northern Chile: (1) early to middle Miocene ignimbrites (20.3 to 15.8Ma), which encompass the Alfabamba and the Huaylillas ignimbrites (Wilson and García, 1962; Lefèvre, 1979; Vatin-

Pérignon et al., 1996; Wörner et al., 2000; Thouret et al., 2004); (2) late Miocene to early Pliocene ignimbrites (10 to 5.5Ma), termed Chuntacala Formation (Tosdal et al., 1984; Sébrier et al., 1988) and Caraveli ignimbrites in Peru (Thouret et al., 2004); (3) Pliocene ignimbrites (5 to 2Ma), termed Sencca Ignimbrites (Lefèvre, 1979; Vatin-Pérignon et al., 1996; Thouret et al., 2004) and; (4) more local Pleistocene ignimbrites (Arequipa area, 1.6 to 0.4Ma; Vatin-Pérignon et al., 1996). The RCI belongs to the Huaylillas ignimbrites sequence. An apparent quiescent period of ignimbritic volcanism of 6Ma in the Arequipa area separates the LJI from the RCI, during which the two presumed major tectonic phases (Quechua II and III) took place. The tectonic depression of Arequipa, which has been filled by two Pliocene ignimbrite sheets (LJI and AAI), therefore existed before 4.9Ma. The tectonic depression was probably formed between 13Ma, which is the age of the RCI, and 4.9Ma, the age of the LJI. The LJI and AAI sheets were emplaced during two ignimbritic pulses only 3Ma apart. The two ignimbritic pulses might be separated by a late Pliocene tectonic phase which has not been defined in the Arequipa area yet.

6.3. Location of vent sources

Determining the location of the sources (vent or caldera) of the older Neogene ignimbrites is a difficult task in the tectonically deformed Western Andean cordillera of southern Peru, which is covered by young and large volcanic edifices.

Thus, the distribution of the Miocene RCI is unknown because it is only exposed in the walls of the Río Chili canyon (Figs. 2 and 3). The LJI sheet geometry suggests a source area located to the North of the Arequipa depression (beneath the Chachani complex or on the Altiplano, north of El Misti): the ignimbrite spreads towards the SW (La Joya) and NE (Sumbay), and at the same time becomes thinner toward the SE (Yarabamba), as shown in Figs. 2 and 3. The geometry of the AAI sheet in the depression and beneath the Pampa de Palacios domes indicates that pyroclastic flows were probably fed by a vent now buried beneath the Chachani volcanic complex (Fig. 2). This hypothesis is also supported by Anisotropy of Magnetic Susceptibility (AMS) measurements (Paquerneau et al., 2003, submitted for publication). Indeed, poles of well-defined foliation planes of magnetic fabric of the AAI reflect flow directions compatible with a source located beneath the southern part of the

Chachani complex. Moreover, the maximum lithic clast-size of the pink unit decreases away from the Chachani volcanic complex from 5.4 cm (on average) in the northern part of the Arequipa depression, to 3.7 cm toward the south (near Uchumayo), and to as little as 2.8 cm to the SSE (near Chilina). This points to a source buried beneath the southern part of the Chachani complex.

The two voluminous ($\sim 40 \text{ km}^3$) Pliocene ignimbrites (LJI and AAI) are probably associated with calderas, as suggested by García et al. (1997). However, no caldera structures are clearly exposed north of the Arequipa depression and around the Chachani complex. A lobate escarpment facing the eastern flank of the Chachani complex on the Altiplano (Fig. 2) was interpreted to be the rim of the “Chachani Caldera” by García et al. (1997). Using the relation between ash-flow eruption volume and caldera area as proposed by Smith (1979), we estimated a caldera area for the AAI (20 km^3) ranging from 10 km^2 for a 1 km depth of draw-down in a magma chamber to 100 km^2 for a 100 m depth of draw-down in a magma chamber. Assuming a circular caldera structure, the diameter of the AAI caldera would range from 3.6 km to 11.4 km and be small enough to be completely covered by the Chachani complex.

7. Conclusions

Four ignimbrites were described, dated, and correlated across the Arequipa basin and on its southern and northern margins:

- (1) The 13.19-Ma-old crystal-rich mLT RCI of an unknown geometry can be correlated with the Huaylillas ignimbrites in southern Peru (e.g. in the area of Chuquiabamba WNW of Arequipa).
- (2) The 4.8-Ma-old LJI has an area of 800 km^2 and a volume of 16 to 24 km^3 . This widespread sanidine and quartz-rich mLT facies ignimbrite ran up and flowed beyond the Arequipa Batholith to the SW. The LJI probably erupted from a source vent located beneath the Chachani volcanic complex.
- (3) The 1.65-Ma-old AAI has an area of 600 km^2 and a volume of 18 to 20 km^3 . It consists of two white and pink mLT units, which filled the Arequipa depression. Field and geophysical evidence point to a source vent buried beneath the southern part of the Chachani complex.
- (4) The early Pleistocene stratified ash and pumice flows of the YT with a volume of 1.5 km^3 originated from a “paleo-Chachani” volcano, north of Nocarani and south of Baquetane volcanoes.

The Arequipa Ignimbrites are intercalated with deposits associated to the post-Oligocene compressive tectonic phases of the Central Andes described by Sébrier et al. (1988); and are coeval with the period of continuous uplift of the Western Cordillera described by Thouret et al. (2004). Subtle compositional differences found in the ignimbrites reflect variations in magmatic differentiation or source melting processes and different degrees of crustal contamination with time. A detailed paleomagnetic and AMS study is presently being carried out on the Arequipa Ignimbrites to help in correlation, location of sources, and mechanisms of transport.

Acknowledgements

Field work was supported by the Institut de Recherche pour le Développement (UR 104, G. Hérial), the IRD office in Lima (R. Marocco, P. Soler), the Laboratoire Magmas et Volcans UMR 6524 CNRS, and OPGC, the Association des Femmes Françaises Diplômées des Universités and by the Instituto Geofísico del Perú in Lima and Arequipa. We thank G. Hartman for XRF and Sr isotope analyses, and K. Simon for trace element analyses with ICPMS. We are also particularly grateful to A. Kronz for EMP analyses. F. Gracia (UNSA Arequipa), F. Legros, O. Macedo (IGP Arequipa), and P. Roperch are thanked for their help and valuable discussions in the field and laboratory. Dr. R. Stewart is acknowledged for his helpful corrections. Finally, we like to thank C. Siebe and an anonymous reviewer for their constructive comments.

References

- Babeyco, A.Y., Sobolev, S.V., 2005. Quantifying different modes of late Cenozoic shortening in the Central Andes. *Geology* 33 (8), 621–624.
- Barker, D.S., 1996. El sillar ocioso. *Bulletin of Volcanology* 58, 317–318.
- Branney, M.J., Kokelaar, P., 2002. Pyroclastic density currents and the sedimentation of ignimbrites. *Memoirs of the Geological Society of London* 27, 51–85.
- De Silva, S.L., Francis, P.W., 1989. Correlation of large ignimbrites – two case studies from the Central Andes of Northern Chile. *Journal of Volcanology and Geothermal Research* 37, 133–149.
- Fenner, C.N., 1948. Incandescent tuff flows in southern Peru. *Geological Society of America Bulletin* 59, 879–893.
- Fisher, R.V., Schmincke, H.U., 1984. *Pyroclastic Rocks*. Springer-Verlag, pp. 187–230.
- Forget, M.E., 2004. Cartographie géomorphologique des phénomènes volcaniques et glaciaires sur le massif du Chachani, Région d'Arequipa, Pérou. Unpublished Physical geography Master thesis, Université Louis Pasteur-Strasbourg I and Université Blaise Pascal-Clermont II. 105 pp.

- Francis, P., Oppenheimer, C., 2004. *Volcanoes*, 2nd ed. Oxford University Press. 521 pp.
- García, W., Landa, C., 1968. Geología del cuadrángulo de La Joya. Servicio de Geología y Minería, 1 mapa color 1/100 000, Lima.
- García, F.F., Chorowicz, J., Legros, F., 1997. La caldera Chachani, gran centro explosivo Plioceno–Holoceno del sur del Perú? Identificación y evolución en imágenes Landsat y Radar ERS. *Sociedad Geológica del Perú*, Vol. Esp. 1, 449–454.
- Gregory-Wodzicki, K.G., 2000. Uplift history of the Central and Northern Andes: a review. *Geological Society of America Bulletin* 112, 1091–1105.
- Guevara, C., 1969. Geología del cuadrángulo de Characato. Servicio de Geología y Minería, Bol. 23, 53 pp., with color map 1 : 100 000, Lima.
- Harangi, S., Mason, P.R.D., Lukács, R., 2005. Correlation and petrogenesis of silicic pyroclastic rocks in the Northern Pannonian Basin, Eastern–Central Europe: in situ trace element data of glass shards and mineral chemical constraints. *Journal of Volcanology and Geothermal Research* 143 (4), 237–257.
- Hildreth, W., Mahood, G., 1985. Correlation of ash-flow tuffs. *Geological Society of America Bulletin* 96, 968–974.
- Hildreth, W., Moorbath, S., 1988. Crustal contributions to arc magmatism in the Andes of Central Chile. *Contributions to Mineralogy and Petrology* 98, 455–489.
- Jenks, W.F., Goldish, S.X., 1956. Rhyolitic tuff flows in southern Peru. *Journal of Geology* 64, 156–172.
- Kaneoka, I., Guevara, C., 1984. K–Ar age determination of the late Tertiary and Quaternary Andean volcanic rocks, Southern Peru. *Geochemical Journal* 18, 233–239.
- Kennan, L., 2000. Large scale geomorphology of the Andes: interrelationships of tectonics, magmatism and climate. In: Summerfield, M.A. (Ed.), *Geomorphology and Global Tectonics*, pp. 167–199.
- Le Maître, R.W., Bateman, P., Dudek, A., Keller, J., Lameyre Le Bas, M.J., Sabine, P.A., Schmid, R., Sorensen, H., Strekeisen, A., Wooley, A.R., Zanettin, B., 1989. A classification of igneous rocks and glossary of terms. Blackwell, Oxford.
- Lefèvre, C., 1979. Un exemple de volcanisme de marge active dans les Andes du Pérou (Sud) du Miocène à l'Actuel. Thèse Université Sciences et Techniques du Languedoc, Montpellier. 555 pp.
- Legros, F., Cantagrel, J.M., Devouard, B., 2000. Pseudotachylite (frictionite) at the base of the Arequipa volcanic landslide deposit (Peru): implications for emplacement mechanisms. *Journal of Geology* 108, 601–611.
- Mahlburg Kay, S., Mpodozis, C., 2002. Magmatism as a probe to the Neogene shallowing of the Nazca plate beneath the modern Chilean flat-slab. *Journal of South American Earth Sciences* 15, 39–57.
- Mamani, M., Ruprecht, P., Hartmann, G., Simon, K., Wörner, G., 2004. Sources from Central Andean magmatism in time and space controlled by crustal composition and thickness. General Assembly, International Association of Volcanology and Chemistry of the Earth's Interior (IAVCEI), Pucón-Chile.
- Mercier, J.L., Sébrier, M., Lavenue, A., Cabrera, J., Bellier, O., Dumont, J.F., Macharé, J., 1992. Changes in the tectonic regime above a subduction zone of Andean type: the Andes of Peru and Bolivia during the Pliocene–Pleistocene. *Journal of Geophysical Research* 97, 11945–11982.
- Mering, C., Huaman-Rodrigo, D., Chorowicz, J., Deffontaines, B., Guillande, R., 1996. New data on the geodynamics of southern Peru from computerized analysis of SPOT and SAR ERS-1 images. *Tectonophysics* 259, 153–169.
- Paquereau, P., Thouret, J.C., Roperch, P., Fornari, M., 2003. Neogene ignimbrites in the Arequipa region (Peru): correlations, flow directions and source location. American Geophysical Union, European Geophysical Society and European Geophysical Union Joint Assembly, Nice, 6–11 April 2003, Abstract and Poster EAEO3-A-10465 (VGP 10).
- Paquereau, P., Fornari, M., Roperch, P., Thouret, J.C., Macedo O., submitted for publication. Paleomagnetic, magnetic fabric properties, and $^{40}\text{Ar}/^{39}\text{Ar}$ dating, of Neogene–Quaternary ignimbrites in the Arequipa area, Southern Peru. Flow directions and implications for the emplacement mechanisms. *Bulletin of Volcanology*.
- Quane, S.L., Russell, J.K., 2005. Ranking welding intensity in pyroclastic deposits. *Bulletin of Volcanology* 67, 129–143.
- Schmid, R., 1981. Descriptive nomenclature and classification of pyroclastic deposits and fragments; recommendations of the IUGS Subcommission on the Systematics of Igneous Rocks. *Geology* 9 (1), 41–43.
- Sébrier, M., Soler, P., 1991. Tectonics and magmatism in the Peruvian Andes from late Oligocene time to the Present. *Special Paper-Geological Society of America* 265, 259–278.
- Sébrier, M., Lavenue, A., Fornari, M., Soulas, J., 1988. Tectonics and uplift in the Central Andes (Peru, Bolivia and northern Chile) from Eocene to Present. *Géodynamique* 3, 85–106.
- Semperé, T., Butler, R.F., Richards, D.R., Marshall, L.G., Sharp, W., Swisher, C.C., 1997. Stratigraphy and chronology of Upper Cretaceous–Lower Paleogene strata in Bolivia and northwest Argentina. *Geological Society of America Bulletin* 109, 709–727.
- Smith, R.L., 1979. Ash-flow magmatism. *Special Paper-Geological Society of America* 180, 5–27.
- Sobolev, S.V., Babeyko, A.Y., 2005. What drives orogeny in the Andes? *Geology* 33 (8), 617–620.
- Streck, M.J., Grunder, A.L., 1995. Crystallization and welding variations in a widespread ignimbrite sheet; the Rattlesnake Tuff, eastern Oregon, USA. *Bulletin of Volcanology* 57, 151–169.
- Sun, S., McDonough, W.F., 1989. Chemical and isotopic systematics of oceanic basalts: implications for mantle composition and processes. *Magmatism in the Ocean Basins*. Geological Society Special Publication, vol. 42, pp. 313–345.
- Thouret, J.C., Finizola, A., Fornari, M., Legeley-Padovani, A., Suni, J., Frechen, M., 2001. Geology of El Misti volcano near the city of Arequipa, Peru. *Geological Society of America Bulletin* 113, 1593–1610.
- Thouret, J.C., Wörner, G., Singer, B., Legeley-Padovani, A., 2004. “Old” valleys in a “young” mountain range. Published abstract and poster, International Association of Volcanology and Chemistry of the Earth's Interior (IAVCEI) General Assembly, Pucón Chile, 14–19 November 2004.
- Thouret, J.C., Rivera, M., Wörner, G., Gerbe, M.C., Finizola, A., Fornari, M., Gonzales, K., 2005. Ubinas: the evolution of the historical most active volcano in southern Peru. *Bulletin of Volcanology* 67 (6), 557–589.
- Tosdal, R.M., Clark, A.H., Farrar, E., 1984. Cenozoic polyphase landscape and tectonic evolution of the Cordillera Occidental, southernmost Peru. *Geological Society of America Bulletin* 95, 1318–1332.
- Trumbull, R.B., Wittenbrink, R., Hahne, K., Emmermann, R., Büsch, W., Gerstenberger, H., Siebel, W., 1999. Evidence for late Miocene to recent contamination of arc andesites by crustal melts in the Chilean Andes (25–26°S) and its geodynamic implications. *Journal of South American Earth Sciences* 12, 135–155.

- Vargas, L., 1970. Geología del cuadrángulo de Arequipa. Servicio de Geología y Minería, Boletín 24, 64 pp., with color map 1 : 100000, Lima.
- Vatin-Pérignon, N., Poupeau, G., Oliver, R.A., Lavenu, A., Labrin, E., Keller, F., Bellot-Gurlet, L., 1996. Trace and rare-earth element characteristics of acidic tuffs from Southern Peru and Northern Bolivia and fission-track age for the Sillar of Arequipa. *Journal of South American Earth Sciences* 9 (1–2), 91–109.
- Walker, J.A., Moulds, T.N., Zentilli, M., Feigensen, M.D., 1991. Spatial and temporal variations in volcanics of the Andean Central Volcanic Zone (26° to 28°S). *Special Paper-Geological Society of America* 265, 139–155.
- Wilson, J., García, W., 1962. Geología de los cuadrángulos de Pachia y Palca. Comisión Carta Geológica Nacional 4 (serie A).
- Wörner, G., Hammerschmidt, K., Henjes-Kunst, F., Lezaun, J., Wilke, H., 2000. Geochronology ($^{40}\text{Ar}/^{39}\text{Ar}$, K–Ar and He-exposure ages) of Cenozoic magmatic rocks from Northern Chile (18–22°S): implications for magmatism and tectonic evolution of the central Andes. *Revista Geológica de Chile* 27 (2), 205–240.
- Wörner, G., Mamani, M., Mercier, R., Kilian, R., 2004. Geochemistry, radiogenic and U-series isotopes in Andean magmas: crustal assimilation and Adakite-like magmatism in the Central and Southern Andes. General Assembly, International Association of Volcanology and Chemistry of the Earth's Interior (IAVCEI), Pucón, Chile.
- Zandt, G., Beck, S.L., Ruppert, S.R., Ammon, C.J., Rock, D., Minaya, E., Wallace, T.C., Silver, P.G., 1996. Anomalous crust of the Bolivian Altiplano, Central Andes: constraints from broadband regional seismic waveforms. *Geophysical Research Letters* 23, 1159–1162.